



Strontium in Al–Si–Mg Alloy: A Review

M. R. Sai Ganesh¹ · Nikhil Reghunath¹ · M. J. Levin¹ · Adarsh Prasad¹ · Sanapala Doondi¹ · Karthik V. Shankar¹ 

Received: 4 February 2021 / Accepted: 25 May 2021 / Published online: 5 October 2021
© The Korean Institute of Metals and Materials 2021

Abstract

The present article reviews the development of cast aluminium alloy with highlights on improvement in the morphological, mechanical, tribological, and ageing properties of Sr modified Al–Si and Al–Si–Mg alloys. Aluminium and its alloys find application in the automobile and aviation industries. The main objective of utilizing aluminium alloys for structural application, manufacturing of pistons and engine block for automobile industries is its lightweight and low density. However, the low hardness of these alloys results in a high wear rate. The main factor that affects the properties of aluminium alloys is its microstructure, morphological behaviour, size of the grain and phase distribution. The morphological modification for these alloys is done through different processing techniques like casting, heat treatment, solutionising, and alloying element addition which augments the mechanical, corrosion, and tribological behaviour of these alloys. Of the alloying element additions Sr has proved to a very effective modifier for the alloy, and hence the method of modification was studied in detail. The unwanted effects especially porosity, being one of the main factors for failure of components, were investigated and methods to reduce it according to many researchers were included. Reinforcing the aluminium matrix with ceramic particles and surface modification also enhances the properties of aluminium alloys. The current article reviews the recent techniques to augment the microstructure, value of hardness, tensile properties, tribological properties, and corrosion behaviour of cast Al–Si and Al–Si–Mg alloys by the addition of strontium. Moreover, this review also focuses on the future scope of these aluminium alloys for structural application in automobile and lightweight industries.

Keywords Al–Si · Al–Si–Mg–Sr · Mechanical behaviour · Tribological behaviour · Hardness · Tensile strength · Phase diagram

1 Overview

Among the numerous types of Aluminium alloys, Al–Si–Mg alloys are known for its superior properties such as stumpy density, superior mechanical and physical characteristics, excellent castability, weldability, and high resistance to corrosion. On that account, these alloys have been seen extensively in the automobile and aerospace field, applications such as piston, engine block, cylinder head, wheel, etc. and even in biomedical applications [1].

The mechanical behaviour of Al–Si–Mg alloy is extremely affected by the morphology of Si particles [2–5]. The microstructural changes of eutectic silicon modified either by Sr addition or by different treatment processes

are critical to enhancing the mechanical properties [6–9], tribological [10, 11], and thermal properties [12] of Al–Si alloy. Sr is observed to alter the morphology of the eutectic Si phase from coarse plate to fine fibrous-like networks. The cause for such modification behaviour was explained by various researchers. One such typical theory of impurity-induced twinning was by Lu and Hellawell [13]. Recently, Shankar et.al [14] using Extended X-ray absorption (EXAFS) spectroscopy and atom probe tomography (APT) probed the region around Sr atoms in Sr modified Al–Si eutectic alloys. Al–Si–Sr ternary intermetallic compounds have a higher influence on the properties of the alloys and hence their stability and thermodynamics were studied by many investigators [15–20]. The isothermal curves and the phase diagrams help indicate useful reactions of these ternary compounds and can ascertain the involvement of these compounds in the solidification of the alloy [16, 18, 19, 21].

However, the addition of Sr is known to result in unwanted porosity, especially after a certain amount of Sr is exceeded.

✉ Karthik V. Shankar
karthikvs@am.amrita.edu

¹ Department of Mechanical Engineering, Amrita Vishwa Vidyapeetham, Amritapuri, India

Researchers have explored the significance of Sr in increasing the porosity of Al–Si alloys [22]. The authors have pointed out four possible causes for porosity (1) Depression of eutectic temperature (2) Variation of surface tension (3) Increase of hydrogen concentration in the melt and (4) Development of oxides in the melt. Considering one of the causes for porosity, that is, surge in H_2 concentration in the melt due to Sr addition, Zhang et al. [23] measured the H_2 content in modified Al–Si alloy using HYSCAN II. The study pointed out the relative ability of Sr on hydrogen pickup in the melt and on the porosity shape after addition. The role of oxides in porosity formation has been investigated in both directionally solidified A356 [24] and binary Al–Si alloy [25]. One such relation of porosity and strontium oxide was studied in depth by Samuel [26]. To reduce the porosity content, Miresmaeili et al. [27] investigated the impact of melt filtration on Sr-modified LM25 alloy. The contribution of these micro-porosities on the mechanical characteristics such as fatigue life of Al–Si alloy was looked into in detail by Lee [28] and the relation among micro-porosity, strain rate, stress amplitude, and fatigue life were studied.

Apart from the change in properties due to Sr modification, researches have also been conducted in areas regarding different treatment processes. One common way to improve the value of hardness, tensile, microstructure, and behaviour of fracture of Sr modified Al–Si alloys was by heat treatment processes [6, 29]. The solution, aging, T6, melt treatment, and the recently investigated HIP treatment have been observed to greatly affect the mechanical properties with change in few primary parameters like holding time and melt temperature [7, 30–35].

The effect of Sr addition, grain refining, pressure, melt filtration, solution heat treatment, T6 heat treatment, HIP treatment, friction stir processing, fatigue and fracture mechanisms, different loading conditions, micro-porosity, and slow cooling rate or solidification rate on the micrograph, fatigue, corrosion, and mechanical characteristics of Al–Si–Mg alloy were reviewed thoroughly.

2 Impact of the Elemental Composition of Sr on Al–Si and Al–Si–Mg

Table 1 lists out the compositions of Sr added in the Al–Si and Al–Si–Mg alloys used in various studies.

3 Isothermal Section and Phase Diagram of Ternary Al–Si–Sr Alloy

To understand the properties of the Sr modified Al–Si alloys, it is important to look at the different ternary phases formed. In recent years many kinds of research have been done to

understand the Al–Si–Sr ternary systems. Until now, 12 ternary phases have been reported by many researchers. They are AlSiSr [15–17, 20], Al_2Si_2Sr [15–20], $Al_2Si_2Sr_3$ [17, 20], $Al_{16}Si_{30}Sr_8$ [20] and the recently investigated 8 other phases, $Al_2Si_3Sr_3$, $Al_2Si_4Sr_3$, $Al_2Si_7Sr_5$, $Al_3Si_7Sr_{10}$, $Al_6Si_3Sr_{20}$, $Al_6Si_9Sr_{10}$, $Al_8Si_3Sr_{14}$, and $AlSi_6Sr_4$, by Garay et al. [20].

3.1 Stability of Phases

The stability of the phases represented by the $Al_xSi_ySr_{1-x-y}$ structures was extensively studied by Garay et al. [20] using first-principle calculations, by calculating the total energy and formation enthalpies as shown in Table 2. As calculated by Garay et al. [20], the formation enthalpy was found to be negative for all the phases except for $Al_6Si_9Sr_{10}$ and $AlSi_6Sr_4$ phases, which had positive values of ΔH_f (formation enthalpies). This confirms that these 10 phases are energetically stable. The most negative enthalpy is observed by Garay et al. [20] in AlSiSr and $Al_2Si_2Sr_3$ and six other (other than $Al_6Si_9Sr_{10}$ and $AlSi_6Sr_4$) phases suggesting that they are likely to be present in the ground state of the system at low temperatures. The Al–Si–Sr ternary phases have crystalline structures with strontium atoms surrounding skeletal Al–Si bonds. The Aluminium coordination number always will be 3 while the coordination number of Si is varied. The ternary phases were found to have metallic behaviour except for $Al_8Si_3Sr_{14}$ intermetallic which has a semi-metallic behaviour. Figure 1 depicts the crystallographic information and unit cell studied by Garay et al.

3.2 Thermodynamics of Al–Si–Sr System

Phase equilibria and thermodynamic properties of phases other than AlSiSr and Al_2Si_2Sr were not investigated in detail by the researchers. The vertical sections along Al–Si₂Sr, Si–Al₂Si₂Sr and 20 at% Sr, the isothermal section at 500 °C in the Al–Si–Sr ternary system was first constructed by Valkhobov et al. [16], using X-ray diffraction and Thermal analysis techniques. The melting point of the Al_2Si_2Sr ternary compound was found out to be 1010 °C by Valkhobov et al. [16]. Hexawell et al. [18] investigated the Al–Si–Sr ternary phase diagram using the differential thermal method, x-ray structural method, and microstructural testing method adopting the thermal analysis. Hexawell et al. [18] constructed the liquidus surface, between 0–7 wt% Sr and 0–20 wt% Si, within the Al–Si–Sr ternary system. The ternary eutectic reaction $L \rightarrow (Al) + (Si) + Al_4Sr$ was observed for Al–13.2 wt% Si–1.8 wt% Sr at 575 °C as depicted in Fig. 2.

Sato et al. [19] explored the aluminium side of the Al–Si–Sr ternary system employing inverse thermal analysis, XRD, and EPMA analysis to develop the Al–Al₂Si₂Sr quasibinary phase diagram as shown in Fig. 3a. Sato et al.

Table 1 Amount of Sr added in Al–Si cast alloys

S. no	Alloy	Sr content	Reference
1	A360 and A413 alloys	300 ppm Sr	[36]
2	Al-7% Si, Al-12% Si, A319 and A356	200 ppm Sr	[37]
3	A356 alloy	Sr ranging from 62 to 820 ppm	[38]
4	Al-11.6% Si	Addition of 0.0375 wt%Sr	[39]
5	A356.2 alloy and Al7Si alloy	0.025 wt% Sr	[22]
6	A356 alloy	Sr 30 ppm	[40]
7	A356 alloy	0.03 wt%Sr	[27]
8	Al-11.5 wt% Si (A413 alloy)	Sr 250–350 ppm	[41]
9	A319 alloy	200 ppm Sr	[42]
10	A356 alloy	0.002, 0.02, and 0.08 wt% Sr	[43]
11	Al–12 mass%Si alloys	0.0450 wt% Sr	[44]
12	Al-6%Mg-3%Si alloy	0.045 wt%Sr	[45]
13	A356 (Al-7Si-0.3 Mg) alloy	AlSr15 modified	[46]
14	Al-12.6Si-0.35 Mg alloy	0.023 wt% Sr	[47]
15	A356	0.022 wt% Sr	[48]
16	Al-10 wt%Si alloys	0.05 wt%Sr	[23]
17	AlSi7Mg0.3 alloy	0.01 and 0.2 wt% Sr	[2]
18	Binary Al-12Si, ternary Al–12Si–Sr, quaternary Al–12Si–0.1Sr–(0.2–1)Mg alloys	0.02 wt% Sr	[49]
19	Al-11.6Si-0.5 Mg alloy	0.023 wt% Sr	[6]
20	A390 alloy	0.04 wt% Sr	[41]
21	Al–3% Si, Al–7% Si, Al–10% Si, Al–12% Si	0.04 wt% addition of Sr	[50]
22	A356 aluminum alloy	0.08 wt% addition of Sr	[51]
23	A319 aluminium alloy	8 to 96 ppm of Sr	[52]
24	Al-12.7% Si-0.04% Sr alloy	43,53,100,200 ppm of Sr	[53]
25	A356	0.02 wt% Sr	[24]
26	A356.1 alloy	0.0007 wt% to 0.0158 wt% in gravity casting and 0.0015 wt% to 0.04% in squeeze casting	[54]
27	Al-7Si-Mg	0.06 wt% Sr	[4]
28	Al–17Si alloy	0.04 wt% Sr	[10]
29	A356	0.04 wt% Sr	[55]
30	A356	120,170 and 250 ppm. Sr	[56]
31	AlSi10Mg	no Sr was added	[30]
32	Al-19Si	Modified using Al-15Sr modifier	[8]
33	Al-13% Si	0.15–0.25 wt%Sr	[57]
34	A319 alloy	70,110 and 500 ppm Sr	[58]
35	A356	50–100 ppm of Sr	[59]
36	Al-12.7 wt% Si	400 ppm Sr	[60]
37	AlSi6.6 and AlSi9.7	170 ppm Sr	[61]
38	Al-10.8%Si	0.014 and 0.03 wt% Sr	[62]
39	A356 and A319 alloys	70, 200, 250 and 600 ppm Sr	[25]
40	Al-7% Si, Al-13% Si and A413.2 alloys	0.02%–0.03 wt% Sr	[63]
41	Al-12Si Alloy	460 ppm Sr	[64]
42	Al-15 wt%Si alloy	80 to 120 ppm Sr	[65]
43	Al-12Si alloy	0.015–0.05 wt% Sr	[66]
44	Al–3%Si–0.04%Sr and Al–12.5%Si–0.04%Sr alloys	200–400 ppm Sr	[14]
45	Al-11.6%Si-0.4%Mg alloy	0.010, 0.015, 0.020, 0.025, 0.030 and 0.0375 wt% Sr	[67]
46	A356 alloy	200 ppm Sr	[9]
47	Al-10 wt%Sr alloy	80–120 ppm Sr	[68]
48	A356 alloy	200–400 ppm of Sr	[69]

Table 1 (continued)

S. no	Alloy	Sr content	Reference
49	AlSi10Mg alloy	400 ppm of Sr	[70]
50	A356 alloy	0.03–0.0426 wt%Sr	[71]
51	Al-5 wt% Si-Sr	50–3000 ppm Sr	[72]
52	Al-12.6% Si	No Sr was added	[13]
53	Al-25%Mg2Si in Situ composite	0–0.3 wt% Sr	[5]
54	A383 alloy	200 ppm Sr	[29]
55	Al-7Si-0.5 Mg alloy	200–600 ppm of Sr	[26]
56	AlSi9	50, 120, 200, 250 and 400 ppm Sr	[73]
57	Al–Si Foundry Alloy	50, 100 and 150 ppm Sr	[74]
58	A356 alloy	No Sr added	[28]
59	Al–Si piston alloys (Al-12Si-3Cu-2Ni-1 Mg)	No Sr added	[75]
60	A356 alloy	No Sr added	[76]
61	Five cast Al–Si–Mg alloys	0.018–0.021%Sr	[77]
62	AC603 ALLOY	No Sr added	[31]
63	Al-7Si–0.6 Mg alloy	No Sr added	[78]
64	A356 alloy	0.013% Sr	[79]
65	A357 alloy	No Sr added	[80]
66	A356 alloy	No Sr added	[15]
67	Al-12.6%Si alloy	No Sr was added	[81]
68	A356 alloy	0.025 wt% and 0.04 wt%Sr	[82]
69	Pure Al, Al-1 wt% Si, and Al-9 wt% Si	200 ppm Sr	[83]
70	A356 alloy	no Sr was added	[84]
71	LMO (99%Al), LM4 (Al–5Si– 3Cu), and LM24 (Al–8Si– 3Cu–Fe)	no Sr added	[85]
72	Al-7 wt%Si and Al-12.5 wt%Si	250 and 350 ppm for the 7 and 12.5%Si alloys, respectively	[86]
73	A356	0.017 wt%Sr	[87]
74	Al-9 wt%Si alloy	no Sr added	[88]
75	Al-Si	0.005 wt%, 0.01 wt%, and 0.03 wt%Sr	[90]
76	A380 alloy	150 ppm Sr	[91]
77	A357 alloy	0.033 wt%Sr	[11]
78	A356 and A357 alloys	0.0143 wt% and 0.0163 wt%Sr A356 and A357 alloys, respectively	[92]
89	A356 alloy	0.02 wt%Sr	[93]
80	A356 alloy	No Sr was added	[94]
81	Al-7Si–Mg (A356) alloy	0.012 wt%Sr	[95]
82	Al-12.2Si-0.3 Mg	0.2 wt% Sr	[131]

[19] observed that the Al–Si–Sr ternary system is divided into Al–Si–Al₂Si₂Sr and Al–SrAl₄–Al₂Si₂Sr regions by the Al–Al₂Si₂Sr quasibinary system as shown in Fig. 3b.

CALPHAD (Calculation of Phase Diagrams) was used to analyse the phase equilibria and thermodynamic properties of AlSiSr and Al₂Si₂Sr ternary phases [22] Wang et al. [15] compared his work with the experimental data from previous studies [16, 19, 21]. The vertical sections were calculated along Al–Si₂Sr, Si–Al₂Si₂Sr, and 20 at% Sr and were compared with previous works [16], as depicted in Fig. 4. The data was found to agree with that of the previous works

of Valkhobov et al. [16], Kauzlarich et al. [21], however, it was observed that the data by Sato et al. [19] deviated by large amounts as shown in Fig. 4a. Wang et al. [15] also constructed the isothermal section of the Al–Si–Sr ternary system at 500°C and the experimental data were found to agree with that of Valkhobov et al. [16]. The Al side of the section clearly shows that there are two of Al–Si–Al₂Si₂Sr and Al–SrAl₄–Al₂Si₂Sr regions divided by the Al–Al₂Si₂Sr quasibinary system which was previously mentioned by Sato et al. [19] in Fig. 5.

Table 2 Crystallographic information and formation enthalpies of all the ternary intermetallic compounds.

Phase	Space group		Pearson symbol	Formation enthalpy (Kj/mol atom)		
	No.	Group		ΔH_f^{LDA} [20]	ΔH_f^{CGG} [20]	ΔH [15]
AlSiSr	187	P-6m2	hP3	−40.85	−43.43	−4538
Al ₂ Si ₂ Sr	164	P-3m1	hP5	−31	−31.38	−32.38
Al ₂ Si ₂ Sr ₃	71	Immm	o17	−42.05	−43.34	–
Al ₁₆ Si ₃₀ Sr ₈	223	Pm-3n	cP54	−16	−16.2	–
Al ₂ Si ₃ Sr ₃	62	Pnma	0P8	−40.29	−36.56	–
Al ₂ Si ₄ Sr ₃	12	C2/m	mC9	−43.18	−38.41	–
Al ₂ Si ₇ Sr ₅	12	C2/m	mC14	−42.87	−38.02	–
Al ₃ Si ₇ Sr ₁₀	193	P63/mmm	hP20	−42.48	−40.41	–
AlSi ₆ Sr ₂₀	6	Pm	mP39	−39.91	−37.35	–
Al ₆ Si ₉ Sr ₁₀	166	R-3m	hR35	1.9	2.1	–
Al ₈ Si ₃ Sr ₁₄	148	R-3	hR35	−29.01	−29.13	–
Al ₂ Si ₂ Sr ₄	12	C2/m	mC11	5.55	7.17	–

Reproduced with permission from Garay et al. [20] and Wang et al. [15] with permission from Elsevier

4 Impact of Sr Addition on the Eutectic Si Morphology

Adding trace levels of Sr has been known to alter the morphology of Si from coarse plate (flake-like) to fine fibrous (root-like) structure and thus improving many mechanical properties such as ductility and strength [26, 38, 50, 71, 97–99]. Zhang et al. [26] observed that a Sr amount of 0.03 wt% is enough for widespread modification of eutectic Si in LM25 alloy. Increased Sr additions, greater than this amount, did not affect the morphology further. Other modification processes include the subjected heat treatment processes, the cooling rate, the grain refiners addition, and also the type of casting. Although this fact of chemical modification by Sr was discovered 90 years back, there has been still no common understanding of this mechanism of Sr modification. According to Zhang et al. [49], the unmodified primary Si is octahedron in 3D after deeply etching the Al matrix as shown in Fig. 6a. At 0.06% Sr addition, however, the typical morphology of primary Si changes to imperfect octahedron with primary dendrites or secondary dendrites as depicted in Fig. 6b. Another significant change that took place is the number of twins. Unmodified Si structure is observed to have little or no twins, however, on Sr modification, the twin density was observed to increase. Quiyang et al. [100] remarked that thermodynamic parameters such as latent heat of fusion were not affected, and therefore it could be argued that the morphology change is a kinetic one rather than a thermodynamic issue. Recently the theories behind this mechanism over the last 80 years were reviewed in detail by Makhlof et al. [101] and Hedge et al. [102].

In non-binary Al–Si–Mg alloys, the intermetallic phases of magnesium are also influenced by the modification by strontium, in particular, the Mg₂Si phase changes considerably in morphology from fragmented phase to skeletal

structure, as noticed by Stunova [70] and Wang et al. [5]. However, heat treatment-induced change (precipitation of Mg₂Si phase) was found to highly influence the mechanical properties rather than change by only Sr modification [31, 49, 96]. The SEM and OM microstructure of Sr modified Al–Si–Mg alloy were investigated by Yanagihara et al. [45]. Primary α -Al phases and Al–Mg₂Si eutectic phase was observed as shown in Fig. 2. Heterogeneous nucleation of eutectic Mg₂Si from hexagonal-plate-like Mg₂Si observed in unmodified alloy changed to homogenous, on Sr addition (0.045 wt%), with very fine square-plate-like Mg₂Si growth. One important observation was, at high magnesium levels it was observed that the effect of Sr modification was lowered [63]. On Mg additions, the eutectic morphology becomes less and less modified in the Sr modified alloy. The reason to which why the Mg addition masks the effect of Sr modification is, according to Joenoes et al. [63] due to the formation of a complex intermetallic compounds of Mg and Sr (Mg₂SrSi₃Al₄) before the eutectic reaction. In the partially modified alloys, at 0.015 wt% Sr modification, the eutectic Si does not completely change into fibrous morphology [67]. Since the flake-like structure remains, Mg₂Si can nucleate and grow on these surfaces into bamboo-shoot shape structures similar to as in unmodified alloys. Hence the nucleation and growth of Mg₂Si crystals remain unchanged at low Sr additions. On increasing the Sr content, eutectic Si undergoes morphology change from flake-like to a very fibrous structure. High-density twins are observed at the silicon fibers [103]. As a result of this shift in eutectic Si morphology, the nucleation of Mg₂Si is severely decreased and the bamboo structure totally disappears and, instead, several white particles are located at the border of the eutectic cells, the scale of which is evidently greater than that of the eutectic cells, as shown in Fig. 7. The other reason for this restraining effect was attributed to the increase in α -Al dendritic

phase due to Strontium addition. This similar phenomenon of increase in dendritic phase was previously found by Zhou et al. [39] in his observations. The increase in α -Al dendritic phase results in increased dissolving of magnesium in the α solution, resulting in a decrease in Mg content, thus restraining the formation of Mg_2Si .

At present the most common classes of theories of modification of Al–Si are.

1. Restricted growth theory
2. Restricted nucleation theory.

4.1 Restricted Growth Theory

4.1.1 Mechanism of Morphology Change in Unmodified Al–Si Eutectic

It was assumed that the flake-like silicon phase was formed by twinning by a process known as the twin plane re-entry edge (TPRE). It was first proposed by Hamilton et al. [104] to describe the growth of germanium dendrites and was later applied to the growth of silicon. In the unmodified Al–Si alloy, according to Kobayashi et al. [105], the nucleation of Si occurs when two groups made up of Si atoms (arranged as tetrahedron as shown in Fig. 8a) join together to form an embryo. After formation, the embryo grows into a vital size nucleus by the addition of Si atoms to its surfaces. As depicted in Fig. 8b, the central mirror plane between two tetrahedrons becomes $\{1\ 1\ 1\}$ twin plane. More tetrahedrons can add to the growing nucleus, which minimizes its surface energy by forming $\{1\ 1\ 1\}$ planes at its corners. The plate/flake-like morphology results when two or more $\{1\ 1\ 1\}$ twin planes triggers the growth of the silicon phase via the TPRE mechanism as shown in Fig. 9.

4.1.2 Mechanism of Morphology Change in Modified Al–Si Eutectic

The Si phase growth in Sr modified alloy, was studied in detail by Lu and Hellawell [81] using TEM analysis. Like the growth of Si seen in Fig. 10, the growth of Silicon is in the jagged fashion of branching. As per Shamsuzzoha et al. [103], the plausible reason for excessive twin intensity was that strontium adsorbs on $\{111\}$ silicon surfaces and lowers the $\{1\ 1\ 1\}$ twin boundary energy. The possible growth mechanism was illustrated as shown in Fig. 11. Twins marked BC rise from Twins AB. Further, the surface marked C acts as nucleation sites for more AB twins and this continues and generates the entire fiber. However as observed by, Lu and Hellawell [81], twin density was more frequent in Impurity modified fibers than in fibers with flake morphology. And quench modification resulted in far lower twins than impurity-modified fibers. This TPRE poisoning

mechanism does not however accurately determine how specifically re-entrant edge poisoning occurs and what it is that decides whether an element may act as a modifier.

Hence, Impurity induced twinning theory was introduced by Lu and Hellawell [13] in 1987 which was the most widely accepted theory to understand the process whereby the chemical modifiers, such as sodium and strontium, act as a poison for otherwise growing atomic layers. As compared to Na modified samples, Sr modification showed a similar twinned structures as shown in Fig. 12, however, the intensity of twinning was less. It was concluded from TEM analysis, that strontium is adsorbed by silicon liquid front, prohibiting the silicon atoms attachment to the crystal and thereby promoted multiple twinning, Fig. 13a. Assuming this type of surface adsorption, as seen in Fig. 13b, a modifier atom (Na or Sr) of sufficient size causes a monolayer step to skip a usual close-packed position and thus collapse into the next alternative stacking sequence, forming a twin. One of the basic principles of Impurity Induced Twinning Theory is that faceted silicon develops mainly by layer growth and not by TPRE mechanism.

Lu and Hellawell [13] determined the optimum ratio of impurity-modifier to matrix atom radii needed for impurity-induced twinning: r_i/r_{Si} to be equal to 1.6457. However, neither Na (ratio of 1.58) nor Sr (ratio of 1.84) was among the best modifiers to satisfy this condition. Also, lithium although having its ideal ratio nowhere close to the suggested value is observed to modify silicon morphology when added in large amounts [107]. Hence these theories regarding the restricted growth rate of eutectic Si due to Sr addition is widely debated by many researchers.

Recently in 2012, Timpel et al. [68] used atom probe tomography (APT), to analyze the elemental distribution in Al–Si alloy with 200 ppm Sr to evaluate the Sr distribution in alloy and its role in modifying the eutectic phase. The findings indicated that Sr co-segregates with Al and Si in the eutectic Si phase in 2 ways: Type I segregation was responsible for the formation of multiple twins in Si crystal and allowed for their growth in different crystallographic directions. The Type II Sr–Al–Si co-segregations were found in internal boundaries of the eutectic Si phase and initiated Al/Si interface. According to Timpel et al. [68], these Sr–Al–Si co-segregations were adsorbed at the solid–liquid growth front of Si at the re-entrant edges and subsequent attaching of Si atoms to the growing crystal by the TPRE mechanism was restricted, as previously shown in Fig. 8b. Due to this restriction of growth of Si crystal, Al phase grows ahead of Si phase thus resulting in morphology change in Si eutectic.

The evidence that Sr is segregating along with Al and the main component Si on an atomic level has shown that the combined effect of these elements has allowed the development of twins rather than only the individual Sr atoms, as illustrated in Fig. 14a. However, as stated by Timpel et al. [68] even though Sr does lead to a higher twin density,

which only indirectly contributes to eutectic modification, it is the Type II segregation that contributes to the branching of Si fibers and not the twinning, as presumed in previous theories [13, 103].

4.2 Restricted Nucleation Theory

On Solidification of Al–Si unmodified, significant undercooling is observed with large interparticle spacing. On addition of modifiers like Na and Sr the undercooling is further increased with a decrease in interparticle spacing Fig. 15. Flood and Hunt [108] observed the microstructure of partially solidified unmodified and modified (with Na) alloys. It was found that Si nucleates ahead of solidifying front as individual eutectic cells on aluminium dendrites. On modification with Na, however the nucleation ahead of the solidification front was not observed, hence the large undercooling in modified alloys. Since the eutectic nucleates ahead of the nucleation front on the aluminium dendrites, the area of the eutectic front is bigger than modified alloys. The interparticle spacing is higher in unmodified alloys due to the fact that the velocity of the interface is much lower than when on modification. Hence, the relation between nucleation kinetics and undercooling was found to be evident from this study. Flood and Hunt [108] constructed a mathematical model describing the nucleation kinetics of the alloy. The author proposed that the transition from faceted to non-faceted eutectic structure happens even at higher growth velocities. In the previous works, the formation of faceted Si occurs through TPPE (Twin plane re-entrant edge) mechanism and the addition of Na causes multiple twinning's (leading to fibrous morphology). However, even at modified Al–Si alloys occurrence of twins was not observed as in the study by Fredrikson et al. [109]. Since different crystal facets or planes grow at different speeds, faceted Si dominates at lower growth velocities. The crystal is therefore confined by the slowest growing faces. At high enough velocities, all the crystal planes grow at the same speed (since the difference between the growth rates is too small) and hence the non-faceted Si structure. Flood and Hunt [108] proposed that the transition from plate-like to fibrous occurs at the same time during the transition from faceted to non-faceted growth. At low velocities, the addition of modifiers like Na or Sr reduces the faceted-non-faceted transition temperature as per in Fig. 16. Hence the transition from faceted to non-faceted is possible at lower velocities.

In the year 2001, Dahle et al. [110] introduced three possible modes of nucleation in Al–Si alloys as shown in Fig. 17. The three modes proposed are: nucleation at or adjacent to the wall and front growth opposite the thermal gradient, nucleation of eutectic on primary Aluminium dendrites, and heterogeneous nucleation of eutectic on nucleant particles in the interdendritic liquid. The effect of

modifier element Sr on nucleation and growth of eutectic in a commercial hypoeutectic Al–Si alloy was investigated by Dahle et al. [58] and Nogita et al. [59]. In the unmodified alloy, it was found that the eutectic Si nucleates adjacent to the primary aluminium dendrites with the same orientation, as shown in Fig. 18a. At the early stages of eutectic arrests, eutectic Si nucleated and grew at the dendrites tips. For Sr levels between 70 and 110 ppm, it was found that the eutectic silicon transformed into fibrous structures as depicted in Fig. 18b and c. Also, the eutectic was found more distributed, filling the large intergranular area and not connected to the aluminium dendrites. The growth and orientation of eutectic grain were independent of the primary α -Al phase. For Sr levels of 500 ppm, the eutectic structure was completely modified, however, maybe due to higher Sr level nucleation of eutectic Si was again observed on the primary phase similar to unmodified alloy. Since the nucleation is reversed after 500 ppm Sr, it was concluded that Sr affects the nucleation mode/kinetics of Al–Si alloys, at low (70 ppm) Sr level, it promotes independent nucleation of Si and at higher levels, the Si particles have become too large (to become effective nucleants) and changed its nucleation mode. Also, it was proposed that this nucleation of eutectic is according to CET (Columnar equiaxed transition). Among the three modes, nucleation on the aluminium dendrites Fig. 17[b] is considered “columnar” and nucleation of independent eutectic grains Fig. 3c, equiaxed. Infact, a mathematical model was proposed by Flood and Hunt [108], for CET. Strontium's part in the nucleation process was in two ways: (1) It increases the undercooling by segregating into the melt ahead of the primary aluminium dendrites and, (2) It influences the nucleants in the melt thereby affecting the nucleation event.

Weimin et al. [111], conducted research on the Si–Si covalent bond in liquid Al–Si alloy and the influence of modification of Sr on it. Using temperature X-ray diffractometer, the existence of Si–Si covalent bond in liquid Al–Si was proved and it was also observed that Sr weakens the bond considerably. Similar research was conducted by Bian et al. [112] using high-temperature X-ray diffraction, and it was observed that due to the weakening of Si–Si bonds, the no. of Si–Si clusters decreased. Since the Si–Si bonds are a potential nucleation site for Silicon, Sr addition caused depression of nucleation of Si atoms causing the aluminium phase to develop before the silicon phase. Using high-energy X-ray diffraction, Shankar et al. [51] examined the influence of strontium upon the morphology of liquid Al–Si alloys. Similar to the research findings by Dahle et al. [58], this study shows that the addition of Sr greatly impacts the liquid structure of these alloys. Adding Sr causes delays in the clustering of Si atoms close to the temperatures at the nucleation event. As per Shankar et al. [51], the inclusion of the low concentrations of Sr to the alloy changes the physical

properties of the liquid, such as the liquid viscosity and the interfacial energy of the inter-dendritic liquid at the final stages of solidification. This delays the nucleation process of the eutectic Si phase, resulting in a substantial under-cooling of the eutectic temperature. Whereby the primary Al phase starts growing and provides conditions at which the Si phase crystallizes spontaneously in the primary Al phase.

4.3 AIP, Bifilms, and β -(Al, Si, Fe) as Nucleation Sites for Eutectic Si

The cause of nucleation of the eutectic phase may also be due to a significant amount of iron impurity present in commercial alloys. According to a recent study by Shankar et al. [113], even trace levels of Fe causes the formation of the iron-containing β -(Al, Si, Fe) phase which plays a significant role in the nucleation of the eutectic phases. In the unmodified alloys, this β -(Al, Si, Fe) phase acts as nucleation sites of eutectic silicon before the nucleation of eutectic Al. Once nucleated, the eutectic silicon grows into flake-like morphology. On Sr modification, the growth of this intermetallic iron-containing phase is interrupted, causing an equiaxed eutectic Al grain to nucleate before the eutectic Si nucleation, and thus, silicon is forced to grow through eutectic Al grains by developing a fibrous morphology as shown in Fig. 19.

Other theories that explained this morphology modification was ternary eutectic theory [14, 37, 44, 72], and nucleation poisoning theory. According to ternary eutectic theory, as observed by Srirangam et al. [14] in hypoeutectic alloys, the Sr bonds with Si atoms, during solidification, forming these $\text{Al}_2\text{Si}_2\text{Sr}$ clusters, thereby deactivating the nucleation sites. This increases the undercooling required for eutectic Si to nucleate in Al–Si. The Sr atoms were seen to segregate in Si-rich regions in modified alloys as depicted in Fig. 20.

The nucleation of eutectic silicon due to AIP (Aluminium Phosphate) was explained by Nogita et al. [114]. It was stated that impurities in the melt strongly influence such types of nucleation. The influence of AIP is illustrated in Fig. [25]. After the formation of AIP at the dendrite-liquid interface, these can act as nucleation sites for the Silicon particles. In the study by Liang et al. [115], thermodynamic description of the Al–Si–P system was investigated, and the ternary eutectic reaction at 577 °C, $L \rightarrow \text{Al} + \text{Si} + \text{AIP}$, revealed many important details. One of them being that even for minute P impurities in the alloy, instead of eutectic Si nucleation directly on the Al dendrites, nucleation through AIP happens indicating its powerful influence on the alloy. These findings were also observed by Zarif et al. [72] observed that the addition of only 5ppm of phosphorous caused a drastic change in nucleation. On addition of Sr, intermetallic $\text{Al}_2\text{Si}_2\text{Sr}$ was observed which nucleated on AIP thus reducing its nucleation potential. The formation

of another compound Sr_3P_2 , which reduced the amount of phosphorous in the melt, was also linked to reducing AIP nucleation potential (Fig. 21).

In a recent study conducted by Y Uchida et al. [44], a similar formation of hexagonal $\text{Al}_2\text{Si}_2\text{Sr}$ with impurity P was identified. Because the formation temperature of $\text{Al}_2\text{Si}_2\text{Sr}$ was thermodynamically estimated to be higher than that of AIP (Aluminium Phosphate) as depicted in Fig. 22, which works as a nucleus of the growth of Si crystal, and $\text{Al}_2\text{Si}_2\text{Sr}$ was incoherent with Si, according to Uchida et al. [44], the formation of $\text{Al}_2\text{Si}_2\text{Sr}$ indicated the suppression of the growth of Si particles under certain P and Sr contents, as seen in Fig. 23. The cause of the formation of a very fine square-plate Mg_2Si phase in Al-6mass%Mg-3mass%Si ternary alloy was also attributed to the formation of AIP as stated by Yanagihara et al. [45]. Hexagonal-plate-like Mg_2Si generated with AIP as nuclei, and the facet growth of eutectic Mg_2Si phase occurred from these hexagonal-plate-like Mg_2Si in the unmodified alloy as shown in Fig. 24a. On 0.045% Sr modification, square-plate-like Mg_2Si was generated at the same time as depicted in Fig. 24b. Sr addition probably decreased the generation of AIP nuclei and hence change in morphology of eutectic Mg_2Si phase was observed, according to the authors [45, 116].

Bifilms as effective nucleation sites were introduced in the studies by Campbell et al. [117, 118]. As shown in Fig 25, it was observed that β -Fe intermetallic nucleates on a bifilm extending the bifilm into near-perfect crystallographic straightness. Also, silicon plates were observed to grow on these bifilms, unfurling these (although not in the same manner as that of β -Fe particle), changing the mechanical properties. The addition of modifiers like Na and Sr, as observed in the popular nucleation theory by Flood and Hunt [108] and Dahle et al. [110], interrupts the formation of eutectic Si ahead of the solidification front. Hence Si formation on bifilms is not feasible anymore, preventing the unfurling of bifilms by Si thus no longer impairing the mechanical properties. Also, bifilms that formed earlier may have attracted alkali and alkali earth metals no longer acting as nucleation sites for silicon. The newly formed bifilms will therefore be more effective in modification. Hence factors like turbulence due to pouring (which is inevitable) which forms bifilms have a higher influence on the modification process as shown in Fig. 25.

5 Effect of Sr on porosity

As previously highlighted, Sr is known to change the eutectic Si morphology from coarse flakes to fine fibrous structures. This plays a significant role in mechanical properties as found by several researchers [48, 49, 66, 80, 90, 120].

However, it was also noted that the inclusion of Sr led to unnecessary changes, such as increased porosity.

Tiedje et al. [86] compared the solidification and porosity formation between unmodified and Sr modified alloy. Just as shown in Fig. 26b eutectic cells nucleate easily and in a high quantity in unmodified alloy castings; therefore, the size of the cells is small. The pores are fine and distributed well, deep in the center of the casting. In Sr modified alloy, the eutectic cell is large and solidified in a mushy manner thus pore formation is observed throughout the casting. The porosity in Al-7 wt%Si alloy was higher than Al-12.5 wt%Si alloy proving that the amount of Si plays a major role in porosity. When they are surrounded by eutectic Si cells pores seem to have a more spherical morphology, as with the case of alloys with higher Si content, instead of being encroached upon by α -Al dendrites which might alter their earlier round shape. Sr modification only further makes the pores more spherical and large. It was seen by Samuel et al. [121] that the pores in unmodified are rounded and are surrounded by eutectic Si grains proving that the spherical shape is formed due larger quantity of eutectic fraction identified in the alloy. Liao et al. [24] studied the formation of porosity due to Sr modification using in situ X-ray imaging and directional solidification technology (XIDS). The formation of pores, their shape, and growth was studied and compared between both unmodified and Sr (0.02wt%) modified A 356 alloy. It was observed that the pore density in the unmodified specimen was higher than Sr modified alloy. However, the pores in Sr modified specimen grew in size and are seen as more spherical and round compared to the unmodified sample. The author claims the increase in porosity to be mainly due to an increase in size rather than the number of pores. Also, the hydrogen level was maintained approximately the same by degassing, and hence the addition of Sr maybe increased the oxide level of the sample acting as nucleation sites for the pore, according to the author. As a result of these increased oxide-containing Sr, more pores nucleate and grow far from the solidification front. These pores hinder the creation of new pores, thereby reducing their total number and overall pore density. Also, these pre-formed pores, having more time to grow, have higher volume fractions, equivalent circle diameters (ECDs), and therefore have a larger scale as shown in Fig. 27.

The main reason for porosity was narrowed down to solidification shrinkage or hydrogen rejection or both combined. Huber et al. [62] studied the impact of interdendritic and burst to feed on the porosity of castings. The interdendritic feeding region seems to be more accountable for the formation of defects in gravity castings whereas the burst feeding region is responsible for defects formations in high pressure die castings. The addition of Strontium in both alloys extended the interdendritic feeding region by 15% while the burst feeding region was getting significantly

shorter, explaining the considerable impact of Strontium on the feeding ability of the AlSiMg alloy and hence its porosity. One other recent factor, according to Liu et al. [60], includes the heat treatment process of the alloy. Liu et al. [60] noted that the heat treatment of Sr modified alloy helped the formation of a large number of microscopic crystal defects in the α -Al matrix. The thermal expansion coefficient of the α -Al matrix is higher than the coefficient of the Si phase and hence during heat treatment of the as-cast alloy, eutectic Si crystals appear to break down in fragile positions, causing cracks. These cracks are filled up by the Al atoms under the capillary force exerted by these cracks, which caused voids in the α -Al matrix. On the spheroidisation of Si due to the modification of Sr, this diffusion of the α -Al matrix is further disturbed to accommodate the change of shape of the Si crystals. Hence due to heat treatment of the alloy, such a large amount of crystal defects is produced throughout the α -Al matrix and even results in its recovery and recrystallization.

Pore growth is governed by a balance between the pressure that encourages growth and the pressures that oppose its formation. This is described in the equation below [83].

$$P_g + P_S \geq P_{atm} + P_H + P_{s-t}$$

where P_g represents the equilibrium pressure of dissolved gases, P_S is the drop in pressure due to solidification shrinkage, P_{atm} is the atmospheric pressure, P_H is the pressure exerted due to Metallostatic head, P_{s-t} is the pressure due to surface tension between pore and liquid. Hence according to the equation above, Pore formation can happen, theoretically, if the pressure due to solidification shrinkage and dissolved gases is greater than that of atmospheric pressure, head pressure, and pressure due to surface tension.

By reducing the P_{s-t} term i.e. by reducing the surface tension between pore and liquid, pore formation can happen. It was first observed by Gruzleski et al. [82] who demonstrated that the presence of 0.1% of Sr in aluminium A356 alloy caused a 10–19% decrease in surface tension and thus promoted the nucleation of pores. If one considers the thermodynamic aspect, reduced surface tension could allow for the early formation of porosities during solidification. However, there is little experimental proof for this theory, and the author [82] suggests that although a decrease in surface tension seems to be one of the factors, it does not alone justify this increase in porosity formation. According to the author, the factors like an increase in oxide inclusions or hydrogen content or a decrease in eutectic temperature seem to be the main cause.

The hydrogen level in the melt varies with Sr addition [23]. A typical plot of unmodified and Sr-modified melt is shown in Fig. 28. It is shown that, after Sr addition, the hydrogen concentration in the alloy increases and reaches a

maximum and thereafter declines. In comparison, the hydrogen content in the unmodified alloy decreases continuously and achieves a stable value, on cooling.

Zhang et al. [23] attributed the increase in hydrogen content, due to the formation of a protective oxide film. In the case of unmodified alloy, pure alumina Al_2O_3 is formed which acts as a stable and protective film from further hydrogen pickup. However in Sr modified alloy a strontium aluminate ($\text{SrO}\cdot\text{Al}_2\text{O}_3$) forms instead, which is less protective than pure alumina, thus increasing the hydrogen pickup. At higher hydrogen content, the hydrogen bubbles are formed at the early stages of solidification. Hence it can be said that these bubbles grow without obstruction in the liquid phase, thus leading to an increase in porosity. There is however some contradiction to this increase in hydrogen content on Sr addition [122].

Bifilms are a folded oxide skin defect that gets introduced into the melt by turbulence [8, 69]. The above observations in the study by Zhang et al. [37] were supported by Atakav et al. [69]. Atakav et al. [69] measured the bifilm index at 1 h holding times. The bifilm index was observed to reduce indicating superior melt quality, possibly due to the formation of $\text{SrO}\cdot\text{Al}_2\text{O}_3$ spinel oxides according to the author. Campbell and Dispinar [85] conducted a reduced pressure test (RPT) to not only assess the melt quality via hydrogen content but also the bifilm content. As the holding time of the melt increases the bifilm index was observed to decrease. As shown in Fig. 29a, these non-wetting surface films are folded over themselves having gas trapped in between them [117]. This forms a defect that acts like cracks in liquid and remains generally for a large amount of time in Al melts. Campbell and Dispinar [85] observed that bifilms were its actual initiator, while hydrogen only further contributes to the growth of pores. Also, in the observations of Dispinar et al. [84] it was noted that compared to hydrogen content, turbulence and vortex (bifilm index increase) have more effect on mechanical properties and porosity. After the bifilm formation due to turbulence, hydrogen gets diffused in and starts expanding the bifilm to form pores. The hydrogen content before and after degassing was noted by Uludag et al. [46] as shown in Fig. 29(b)

These contradictions by researchers [85, 122] regarding hydrogen involvement in porosity, led to believe that depression in eutectic temperature is the main cause. In 2000, Lee et al. [22] conducted in-situ observations on the influence of Sr on the porosity formation, its nucleation, and growth using the XTGS (X-ray gradient stage) technique. Sr addition causes lowering of eutectic temperature, resulting in more time for the growth of pores. However, CM Dennis et al. [83] claimed that if the increase in porosity, on Sr addition, was due to eutectic nucleation, these changes should also include eutectic Si i.e. these variations must only happen in alloys with a substantial percentage of eutectic in their

microstructure. Since most of the microstructure consists of the eutectic Si phase, this modified phase should exert an influence on the porosity according to the author CM Dennis et al. [83]. In the author's observations, it was found that pore morphology in commercially pure aluminium (Al-1 wt%Si) in both unmodified and Sr alloyed does not defer much. However, in Al-9 wt%Si alloy, the pore morphology and distribution significantly changes on Sr addition proving the involvement of Si eutectic. According to this study, a change in the mode of eutectic nucleation happens i.e., eutectic grain nucleates in the liquid independently in Sr modified alloy rather than at the tip of α -Al dendrites, as shown in Fig. 30. These eutectic grains in large sizes trapping liquid pools, resulting in pores on the eutectic grain boundaries distributed all over the casting. Therefore it can be said that, in unmodified alloys, the pores would be concentrated at the centre of the hot spot, while the alloys modified by Sr would have the pores scattered throughout the casting.

Oxide inclusions can also act as nucleation sites for pores and might allow pores to form at inferior gas pressures P_g or hydrostatic shrinkage pressure P_s . Samuel et al. [25, 121] using optical micrographs in 250 ppm Sr modified, Al-12%Si alloy, through higher magnification, several white particles later identified as AlSrO and platelet fragments of β - Al_5FeSi was also identified in the interior of the pore. Aluminium oxide, Al_2O_3 films formed in the unmodified alloy are very active in creating porosity. These pores are formed deep in the casting and can also combine with each other by oxide films. Sr modification leads to Strontium oxides formation, mainly Al_2SrO_3 . The negative free energy of Al_2SiO_3 was found to be higher than that of Al_2O_3 indicating that these strontium oxides can form easily on Sr addition. The pores were formed during melting and high affinity of Sr to oxygen and are round, regular, and are surrounded by eutectic Si regions. The oxides are generally very difficult to remove by degassing and hence filtration by fine ceramic foam filters is suggested to inhibit their passage into casting. Shabestari et al. [27] researched the effect of exposure time of melt Sr modified A356 alloy in an oxidizing atmosphere. It was found that a relatively short exposure times, the oxides were mainly Al_2O_3 and $\text{Al}_2\text{O}_3\cdot\text{MgO}$. The strontium oxides were not visible at the surface of the alloy. However dispersed particles of the phase $\text{Al}_2\text{Si}_2\text{Sr}$ were found and it was postulated that this phase may cause porosity in the alloy. Further research on the effect of $\text{Al}_2\text{Si}_2\text{Sr}$ was however not carried on the porosity formation. The presence of more than 50% Strontium oxides was clearly observed after longer exposure times in the surface layer. Melt filtration was especially found to be effective in reducing the porosity formed by these strontium oxides. One such filtration technique, the prefil (pressure filtration) technique was used to monitor the cleanliness of the melt. It was found that Al_2SrO_3 oxides are

formed for Sr concentrations as low as 30 ppm and is always related with the Al_2O_3 elements as shown in Fig. 31b

Apart from degassing to reduce the oxide or hydrogen content, hot isostatic pressing (HIP) treatment was found to be effective in reducing porosity, [30, 80]. W Schneller et al. [30] Conducted HIP treatment on selective laser melted AlSi10Mg alloy and observed porosity decreased by 64% and maximum pore diameter by 11% compared to as-built alloy Fig. 32.

6 Effect of Sr Addition and Different Treatment Processes on Mechanical Characteristics

Change in the mechanical characteristics is generally due to morphological changes in the alloy, either by a modifier or solidification time or the treatment processes involved. Among the microstructure changes by Sr additions, change in Si morphology mainly defines the property change in Al–Si alloy. The effect of Sr and Mg content and its influence on tensile, yield strength, elongation, and hardness properties are illustrated briefly in Fig. 33, by Hekimoglu et al. [49] and other studies show similar results. As per the study, in ternary alloys the following observations can be made:

1. The hardness values increased on Sr addition possibly because of the breakdown and increased homogeneous scattering of the eutectic Si particles.
2. An equivalent increase in tensile values, as well as elongation, was identified in the alloy due to a shift in Si morphology from plate form to the fibrous form
3. The yield strength wasn't considerably improved on Sr addition

After 0.1 wt%Sr the properties decreased gradually. Change in the morphology of Si particles may have caused this decrease in hardness. In quaternary Al–Si–Sr–Mg alloy, the hardness on Mg addition gradually increased because of solid solution strengthening by the dissolution of Mg in Al-rich dendrites as well as due to the effect of precipitation of Mg_2Si intermediate phase on the microstructure as indicated by Hekimoglu et al. [49] in Fig. 33b. However compared to ternary alloy, elongation to fracture decreased continuously on Mg additions. As noted by the researcher, the decline in the properties of both ternary and quaternary alloys at high Sr and Mg content was mainly because of the presence of Al_4Sr or Mg_2Si intermediate phases within their microstructures.

6.1 Hardness

The hardness of Al–Si alloy does not get affected much by the addition of Sr, compared to other mechanical properties. Levels of Sr up to 0.06% were observed to decrease the hardness by Rodriguez et al. [66] as shown in Fig. 34b. Many researchers [3, 42, 123] preferred different treatment processes compared to eutectic modification by Si. Table 3 lists the different treatment processes and their effect on the value of hardness of the alloy. After the T6 heat treatment process, the microstructure observed contained a mixture of eutectic $\alpha(\text{Al})$, Mg_2Si , Si particles, and some Fe impurities [124]

6.2 Tensile Properties

Ductility and tensile values were fairly improved by Sr addition according to many researchers [3, 4, 9, 36, 66, 90, 125]. Figure 2a shows the relation between the Sr content and the mechanical properties as observed by Rodriguez et al. [66]. The yield strength alone is marginally unaffected by Sr addition. It was observed that the yield strength roughly remains constant after Sr additions by most of the researchers [9, 29, 48]. Far more, studies show Mg content has a higher impact on yield strength values [48]. The inclusion of Sr modifies the eutectic Si particles from needle-shaped to fine fibrous morphology, thus helping to reduce the stress concentration at the sharp corners of the silicon needles [29]. The limit to which these properties can be improved was found to be 0.2 wt%Sr after which the tensile properties were observed to decrease. This was because of the formation of Al–Si–Sr intermetallic particles (mostly $\text{Al}_2\text{Si}_2\text{Sr}$ phase) which would lower the fine Silicon content which would decrease the strengthening effect [3]. Fading of Sr is generally observed for longer holding times of 17 h due to the formation of $\text{SrO}:\text{Al}_2\text{O}_3$ spinel oxides because of Strontium's high affinity to oxygen [26, 36, 65, 69, 126]. The fibrous Si morphology after the addition of Sr at 5 min of holding disappears after 60 min of melt holding because of oxidation of Sr [65]. Its mechanical properties are therefore observed to decrease for longer holding periods due to the reduction in the level of Sr as shown in Fig. 38.

Osório et al. [88] compared the secondary dendrite arm spacing between unmodified and Na-modified alloy, to ascertain its effect on mechanical properties. The dendrite arm spacing seems to be unaffected by modification, although an increase in mechanical properties can be seen. This was explained by stating that extensive distribution of $\alpha\text{-Al}$ phase/fibrous silicon particles boundaries, hinders crack initiation, and hence there is less possibility for fracture. The degree of continuity within the Al matrix process, notably in eutectic regions, also increased with the modification of Sr [29]. The increase in elongation was, as stated by

Table 3 Influence of various processes on the tensile strength, yield strength, and elongation of the alloy

S.no	Treatment process undergone	Author name & Reference	Major conclusions
1	Solution treatment	Lin et al. [6]	For Al-11.6Si-0.5 Mg alloy, the hardness was seen to increase continuously with an increase in holding time. The author proposed a range of 4 to 7 h at temperatures from 535 °C to 545 °C for an ideal increase in hardness versus production efficiency. At a temperature greater than 535 °C the hardness values decrease due to coarsening of eutectic silicon. Figure 35
		Lin et al. [7]	The micro-hardness of Sr alloyed LM 25 was studied at different solution times. At the early stages of solution hardening at 540 °C and 1 h, it was observed that a large amount of the branched and needle-like Si particles dissolved and ruptured, while only a few spheroidized eutectic Si particles were formed. On increasing the time of solution to 8 h, small particles, by diffusion, to reduce the surface energy, dissolve and migrate to Si particles of larger size from the α -Al matrix. There is therefore a decrease in the concentration of Si in the α -Al matrix. However, because of the rapid dissolution of the Mg-containing phases, the concentration of Mg atoms in the α -Al matrix increases considerably. Solution Strengthening of Mg atoms was greater than Si atoms, so there is an initial improvement in the micro-hardness of the α -Al matrix. At higher solution times, Mg atoms prefer to diffuse towards pores, causing a decrease in Mg concentration at the α -Al matrix, and thus a decline in micro-hardness is observed
2	T6 treatment (solution treatment + artificial aging)	Sangchan et al. [3]	A considerable increase in hardness can be obtained on T6 treatment. The author explains the cause for this increase to be due to the formation of a fine Mg ₂ Si phase. Figure 36
		Travitas-Medrano et al. [42]	The highest values of micro-hardness were obtained for T6 treatment at 170°C and 8 h
3	T4 treatment (solution treatment + water quenching)	Travitas-Medrano et al. [42]	T4 treatment was found to increase the hardness when compared to as-cast alloy. T6 treatment (which included artificial aging) was found to increase the values of hardness further
		Osório et al. [88]	Hardness values along with other mechanical properties were observed to increase considerably after T4 treatment. However, the effect of modifier on increasing the properties was found to be masked by the T4 treatment process, i.e., the values of unmodified heat-treated, modified heat-treated, and only modified alloy were found to vary little

the authors [29, 90], because of the fine morphology of Si particles. The microstructure of Sr modified alloy generally constitutes primary α -Al phase equiaxial rosettes surrounded by a more refined eutectic Si phase. The sharp corners of the coarse Si particles serve as stress elevators leading to easy crack formation in the alloy, in the unmodified alloy [10, 29]. Another cause for this improvement in UTS was, as according to H Liao et al. [39] increase in α -Al content in near eutectic Al–Si alloy, however, no further explanation was given as to the cause for this phenomenon. Dimple formation

with fine cleavage facets was observed in the grains suggesting the occurrence of plastic deformation before fracture [10]. Fracture analysis by Hafiz et al. [90] reveals that the unmodified alloy has, at its longitudinal sections, a needle-like Si structure similar to its surface microstructure can be observed, indicating brittle fracture. Sr modified alloy, however, exhibits ductile fracture and the fractured surfaces were found smoother in modified alloys indicating a surge in ductility of the alloy. In the recent study by Liu et al. [29], a relation between the roundness and size of Si

particles with the mechanical properties was observed in the Sr modified high-pressure die-cast A383 alloy. The presence of Sr in the alloy alters the morphology of the eutectic Si to a more rounded microstructure. A linear relationship can be observed for elongation with increased roundness and size of Si (which improved with Sr additions) as illustrated in Fig. 37b, d. However, the yield strength has little to no change on Sr addition as observed in Fig. 37a, c; similar to the observations made by several researchers [9, 48].

It was generally stated by Uludag et al. [46] that by degassing the melt, the melt quality improves, and hence the bifilm index decreases, thus increasing the mechanical properties. The effect of porosity, due to the formation of bifilms by turbulence, on the mechanical properties was

however observed by Uyaner et al. [64] to be insignificant. The properties instead heavily depended on the microstructure of the alloy. It was found that the finer the micrograph the higher the tensile values. Also, the ductility is improved regardless of the amount of porosity in the casting. The variation in mechanical properties like UTS and elongation are shown in Fig. 39. Table 4 shows the details of previous studies on the influence of various process on the UTS, YS and ductility of the alloy.

6.3 Impact Toughness

The impact strength of Al–Si alloys is dependent on the microstructure which is predominantly focused on

Table 4 Influence of various processes on the tensile strength, yield strength, and elongation of the alloy

S. no	Process undergone	Author name & Reference	Major conclusions
1	Type of casting: squeeze cast and gravity die-cast	Shih et al. [54]	The mechanical properties of heat-treated as-cast were superior by 15–30% in squeeze castings compared to gravity die-cast alloys. Treatment processes such as T6 treatment increased the tensile strength by 30% in gravity castings and by 10% in squeeze castings
		Hafiz et al. [90]	The fracture properties were investigated using Optical and SEM micrographs of the fractured specimen. It was observed that the fractured surfaces of the squeeze cast alloys are much smoother than the die-cast alloys indicating higher ductility in the former
2	T6 treatment	Sangchan et al. [3]	T6 treatment however was found to improve only the UTS of the alloy (both modified and Sr modified), whereas the ductility decreased. The explanation for such behavior has been the formation of fine Mg ₂ Si phase and iron intermetallic β-(Al, Si, Fe) during heat treatment
		Jiang et al. [96]	An increase in UTS and ductility was noted by about 291 MPa and 4.45% increase respectively. The L-shaped Mg ₂ Si is modified into a fine spherical shape with the inclusion of the extruded Sr
		Lin et al. [6]	An optimum factor considering the T6 treatment process for Al-11.6Si-0.5 Mg was solutionizing for 6 h at 535 °C, and aging was conducted for 6 h at 160 °C, wherein the maximum tensile, yield strength and elongation values were observed to be 348 MPa, 236 MPa, 6.5% respectively
3	T4 treatment	Osório et al. [88]	On T4 treatment (solution treatment at 540°C for 6 h and then water quenching), the UTS and elongation were found to increase considerably. Spheroidization of Si particles which reduces stress concentrations were found to be the primary cause for this increase. However, the effect of modifier on increasing the properties was found to be masked by the T4 treatment process, i.e., the values of unmodified heat-treated, modified-heat-treated, and only-modified alloy were found to vary little. Hence the author preferred eutectic modification only when compared to T4 heat treatment for the increase in properties for better cost-efficiency
4	Solution treatment	Samuel et al. [9]	On solution treatment (at 540 °C at 0, 8, 40, and 80 h, then ageing done at 155°C for 5 h), the UTS and yield strength of the unmodified and the Sr added alloy increased until 8 h holding time, after which the values remained constant. The increase in UTS was mainly due to precipitation of the Mg ₂ Si phase and change in Si morphology (spheroidisation). Yield strength had no considerable change, however, the ductility was improved in both the unmodified and Sr added alloy
5	Bendability tests	Marzouk et al. [48]	The author carried out both uniaxial tension tests and V-bend tests on A356 alloy. As observed in previous kinds of literature, the ductility values showed a decent improvement on Sr addition. Although both unmodified and Sr-added A356 alloys have inferior bendability compared to most wrought aluminium alloys, alloy modified with Sr is observed to have improved bendability values. The poor bending of the unmodified alloy was due to factors like the larger size, random distribution, and the elongated shape of the Si particles

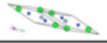
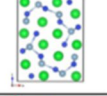
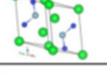
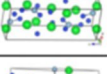
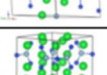
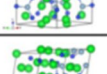
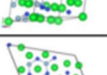
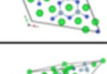

Phase	Unit cell	Space group		Pearson symbol
		Number	Group	
$\text{Al}_2\text{Si}_2\text{Sr}_3$		71	Immm	oI7
$\text{Al}_2\text{Si}_3\text{Sr}_3$		62	Pnma	oP8
$\text{Al}_2\text{Si}_4\text{Sr}_3$		12	C2/m	mC9
$\text{Al}_2\text{Si}_7\text{Sr}_5$		12	C2/m	mC14
AlSi_6Sr_4		12	C2/m	mC11
$\text{Al}_3\text{Si}_7\text{Sr}_{10}$		193	P63/mmm	hP20
$\text{Al}_6\text{Si}_9\text{Sr}_{10}$		166	R-3m	hR35
$\text{Al}_6\text{Si}_{13}\text{Sr}_{20}$		6	Pm	mP39
$\text{Al}_8\text{Si}_3\text{Sr}_{14}$		148	R-3	hR35

Fig. 1 Details on crystallographic and unit cells of the $\text{Al}_x\text{Si}_y\text{Sr}_{1-x-y}$ structures. Reproduced with permission from Garay et al. [20] with permission from Elsevier

modification by the modifier, melt treatment process, and solidification parameters. Hafiz et al. [90] investigated the influence of the cooling rate and Sr concentration upon impact toughness of Al–Si alloy. The casting process was conducted in two molds: Steel and graphite and the Sr content of 0.005 mass%, 0.01 mass%, and 0.03 mass%

were added. It was found that Sr modifications improved the toughness regardless of the cooling rate, but greater improvement in impact toughness by 629% increase was seen in graphite mold (low cooling rate) compared to that of 441% in steel mold (higher cooling rate). However, the highest values of toughness obtained were seen in the case of a faster cooling rate in steel mold as depicted in Fig. 40. The increase in impact toughness on Sr modification was due to, according to Hafiz et al. [90] and Mohammed et al. [62], a change in eutectic Si morphology to a well fibrous structure. This is because a change in morphology of Si increases the maximum bending stress before the crack initiation and decreases the crack growth rate, hence increasing the energy required for crack propagation. Mohammed et al. [62] noted that the presence of iron contributes to increased precipitation of β -Fe which behaves as a crack nucleation region, significantly decreasing the impact toughness. As seen in Fig. 41, crack initiation and propagation energy of Sr modified alloy (RM) increased by 28% from 4.3 J to 5.5 J due to a change in Si morphology from faceted to fibrous Si. The increase in crack propagation energy (of about 55%) was due to the smaller size of the Si particles, which reduced the likelihood for the crack to encounter a brittle Si particle in the now ductile matrix. Solution heat-treatment of the unmodified sample was found to increase the total absorbed energy by about 213%. However, this increase in impact strength in the unmodified alloy was far greater than that due to Sr modification which only increased the energy by 28%. Hence solution treatment was found to be a better alternative compared to modification for superior impact characteristics. The combination of both Sr modification and solution treatment, nonetheless lead to a further increase by 226% of the total absorbed energy. According to Mohammed et al. [62], this was owing to the dissolution of fibrous eutectic silicon into smaller, rapidly spheroidised, and coarse segments.

Fig. 2 Liquidus curve of Al–Si–Sr system. Reproduced with permission from [18] with permission from Cambridge University Press

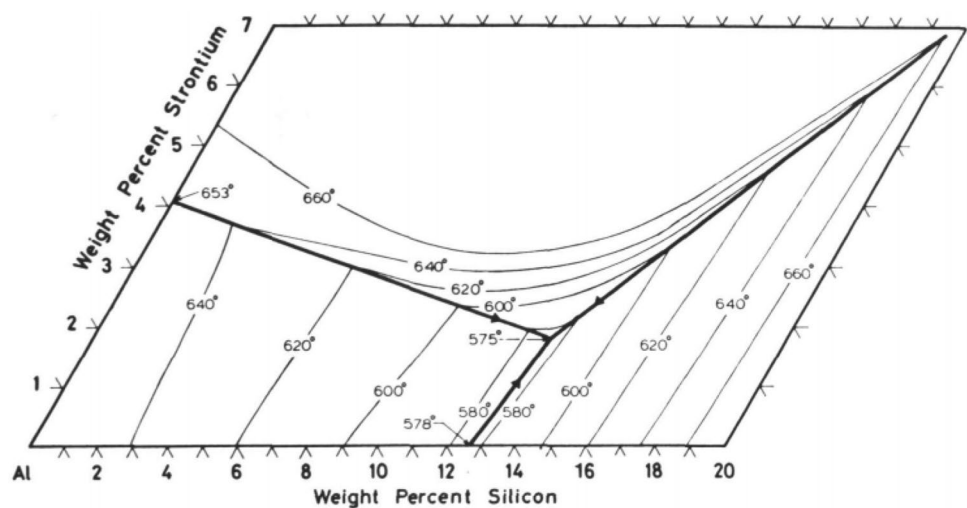


Fig. 3 **a** The phase diagram of Al–SrAl₂Si₂ quasibinary system by Sato et al. [19] (Reproduced under the terms of the Creative Common License) and Vakhobov et al. [16] (Reproduced with permission from [16] with permission from Russian metallurgy (Metalli.)) **b** Corner of Al–Si–Sr ternary system by Sato et al. [19]

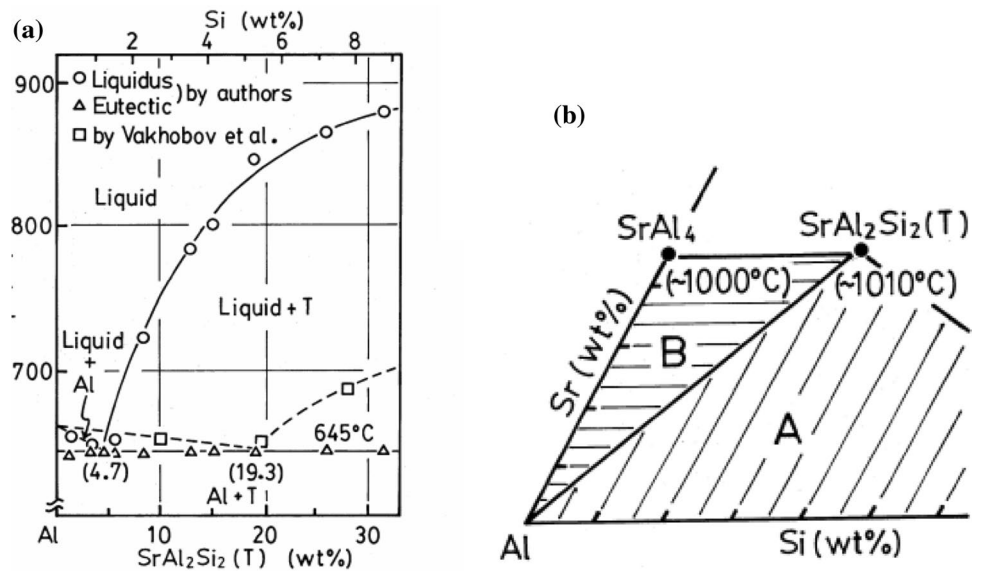


Fig. 4 Vertical sections of **a** along Al–Si₂Sr, **b** along Si–Al₂Si₂Sr, and **c** with 20 at% Sr by Wang et al. [15] (Reproduced with permission from [15] with permission from the Elsevier) compared with previous works [16, 19, 21]

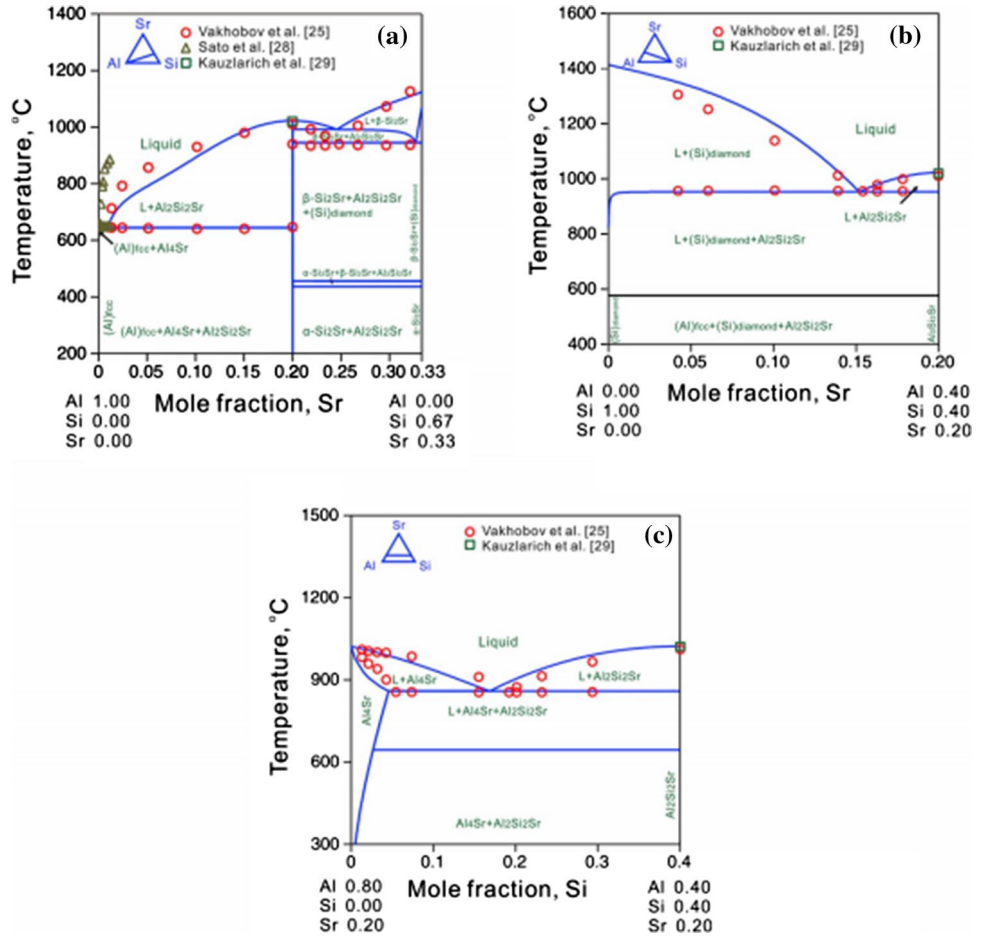


Fig. 5 Isothermal section at 500 °C of Al–Si–Sr ternary system **a** over entire composition **b** Al-rich corner of the section, when compared with experimental data as reproduced with permission from [16] with permission from Russian metallurgy (Metalli.)

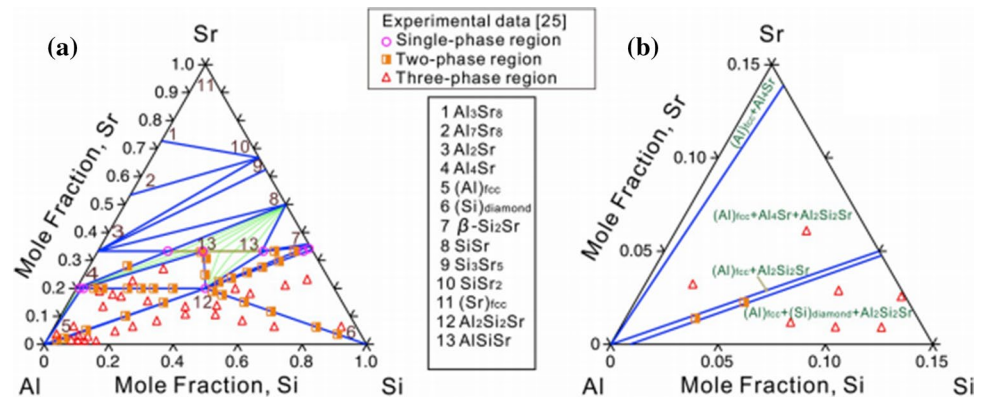


Fig. 6 Morphology of octahedral primary Si: **a** Without Sr **b** with 0.06% Sr. Reproduced from [49] with permission from the Springer Nature

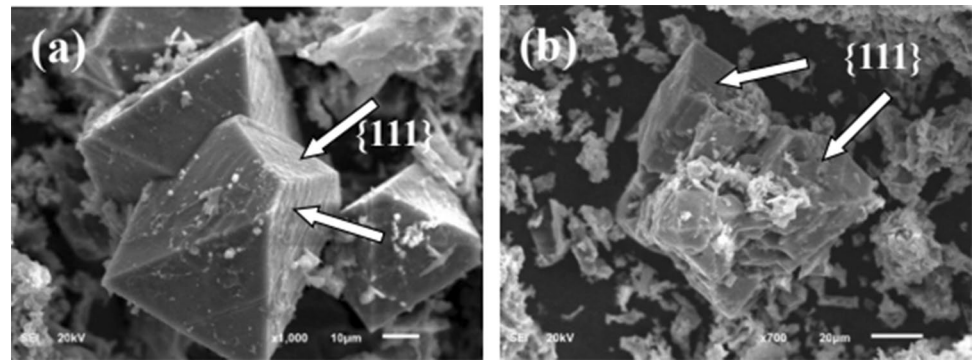
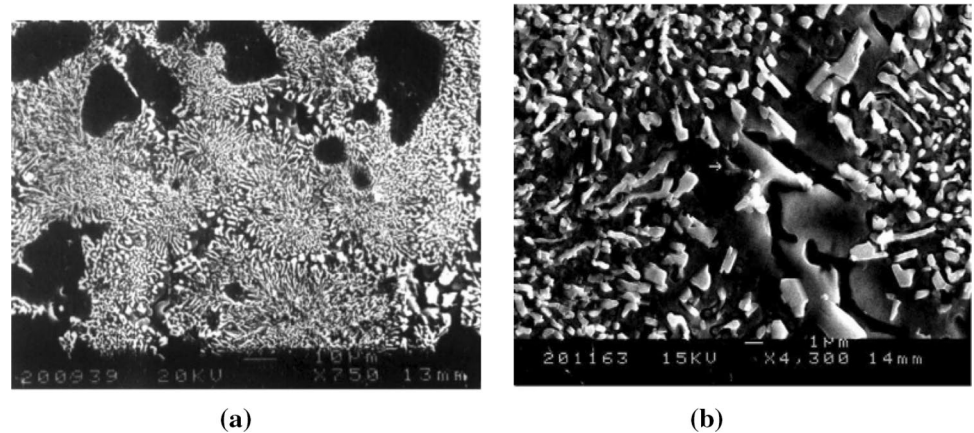


Fig. 7 SEM image of the eutectic cell boundary zone in an Al–Si–Mg alloy with 0.0375% Sr modification at **a** low magnification; **b** high magnification, as observed by Hengcheng et al. [67]. (Reproduced from [67] with permission from Elsevier)



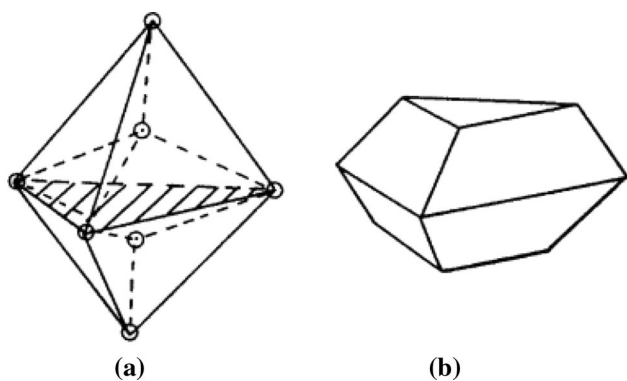


Fig. 8 **a** Tetrahedron with {1 1 1} mirror plane (hatched) made of Si atoms **b** Truncated tetrahedron at later stage growth. Reproduced from [105] with permission from Springer Nature

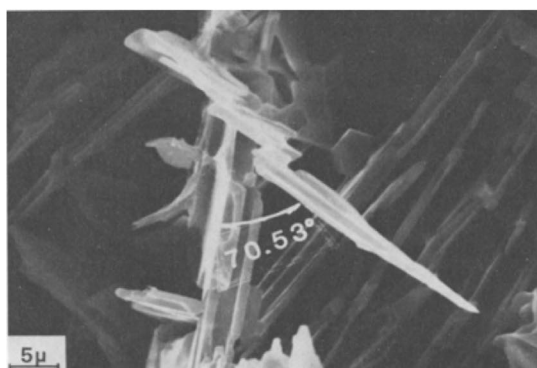
6.4 Fatigue Properties

Pistons in engines and cylinder heads are in constant exposure to cyclic loadings at high fluctuating temperatures. Hence, a need to enhance the fatigue resistance of the alloy is very important. At low temperatures, the fatigue damage

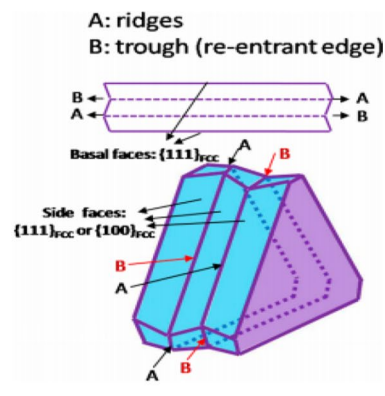
is mainly caused by cracking of primary Si due to piling-up of dislocations, and by Si/Al phase-matrix debonding due to increased vacancy formations at high temperatures [75].

Fatigue failure is generally associated with casting defects in the microstructure. Using a low-power stereo microscope fracture surfaces of fractured specimens were studied by Davidson et al. [31]. In all the cases, the fatigue started either from shrinkage pores or near to the surface of the specimen. The effect of micro-porosities on the fatigue life is dominant at varying stress amplitude at a given strain rate [28]. However, the micro-voids at the crust or the circumference of the sample were found to be much more significant than the micro-voids at the cast interiors, even though the latter acts as crack initiating positions. In the base alloy (no eutectic modification), Schneller et al. [30] found a decrease in porosity (by about 64% compared to as-built alloy), on Hot isostatic pressing (HIP) treatment, and hence the cast defects were no longer responsible for crack initiation. Crack initiated near the subsurface of HIP treated alloy. After HIP treatment and subsequent annealing, the formation of Si agglomerations and needle-shaped iron-rich intermetallic phases were found to restrict the crack growth, and hence

Fig. 9 **a** Faceted silicon flakes in the unmodified alloy. Reproduced from [13] with permission from the Springer Nature, **b** schematic representation of cross-section and the structure of platelet with two parallel {111} twin plates. Reproduced from [106] under the terms of the Creative Common License



(a)



(b)

Fig. 10 Representation of growth of silicon flake by twinning. Reproduced from [16] with permission from the Elsevier

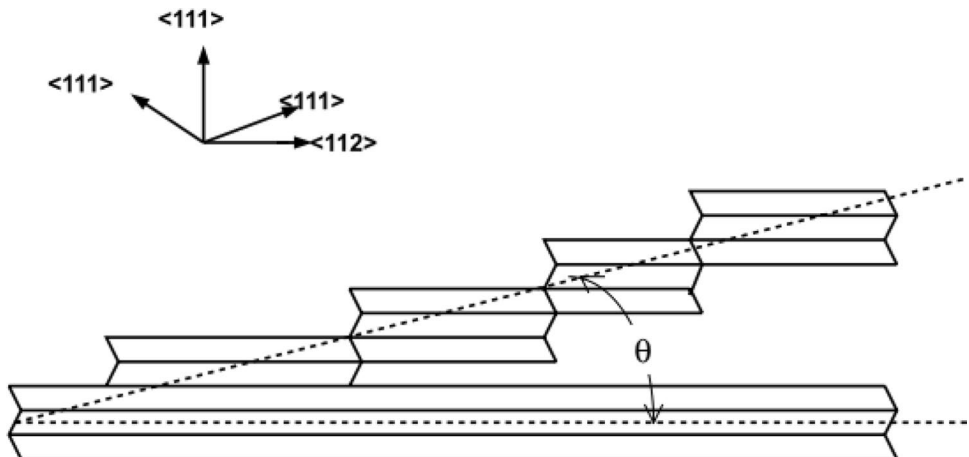


Fig. 11 Representation of twins and their growth in a modified Si fiber. Reproduced with permission from [103] with permission from the Taylor & Francis

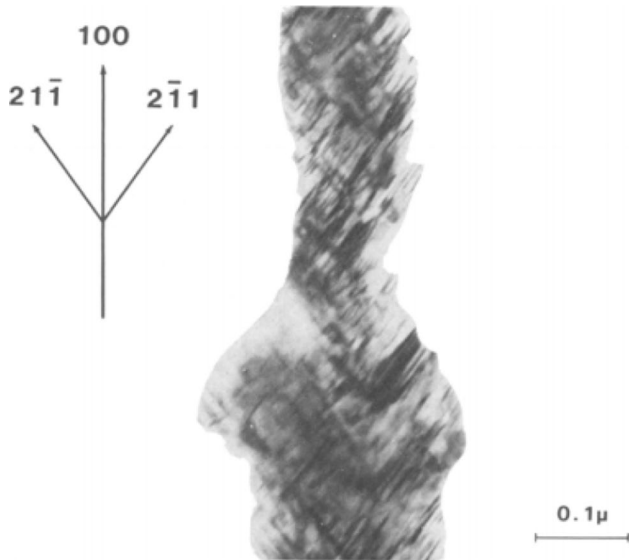
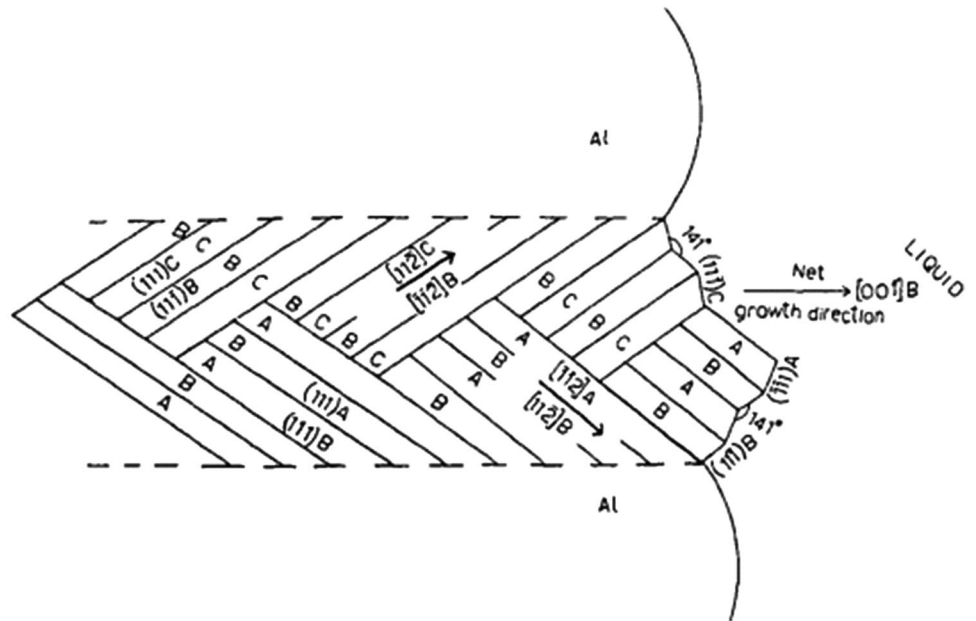


Fig. 12 Silicon modified fiber modified aluminium–silicon eutectic. Reproduced from [13] with permission from Springer Nature

the no. of cycles to failure was observed to increase in the as-cast alloy, as shown in Fig. 42. However, HIP treatment on the Sr modified alloy produced no considerable increase in fatigue life [80]. Sr modifications, which refined and spheroidised the eutectic Si particles, were found to instead increase the fatigue growth rate possibly due to an increase in porosity, as shown in Fig. 43.

Elevated temperatures were observed to reduce the amount of defect in the alloy [127]. This is due to the increasing uniformity of the plastic deformation and the refining of the microstructure which increases the resistance to crack propagation. However, with rising temperatures, crack density increases as precipitate phases become unstable, which at the same time facilitates fatigue damage and cracking. Fatigue damage generally depends on the ability for crack formation and crack initiation. Fatigue cracking exponent, β , which is the property that resists the formation of micro-cracks is higher at low temperatures. However, fatigue toughness, which resists the crack propagation, is observed

Fig. 13 Representation of a adsorption of impurity atoms at monolayer steps on a growth interface, **b** 011 Plane projection showing a modifier atom (black) of a particular atomic radius could stimulate twinning by making the growth step to take an alternative {111} stacking sequence. Reproduced from [13] with permission from Springer Nature

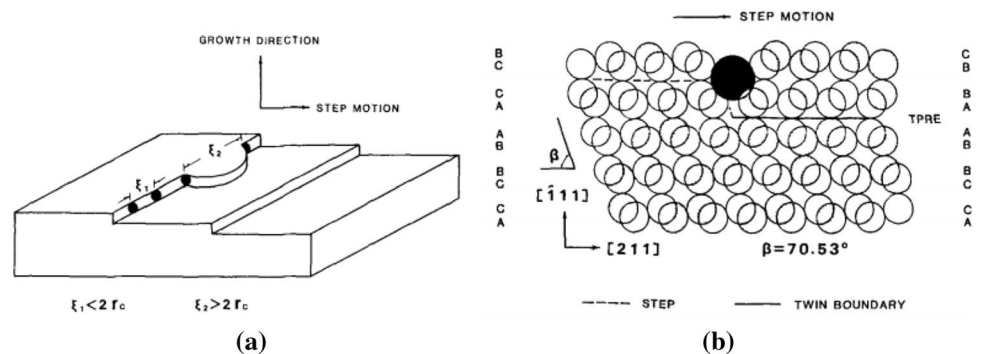


Fig. 14 Representations of $\{0\ 1\ 1\}$ plane projection of eutectic Si phase at locations of: **a** type I Sr–Al–Si co-segregation; **b** type II Sr–Al–Si co-segregations. Reproduced from [68] with permission from the Elsevier

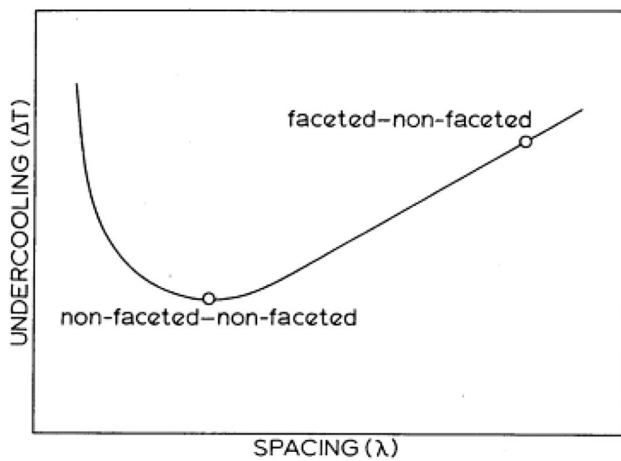
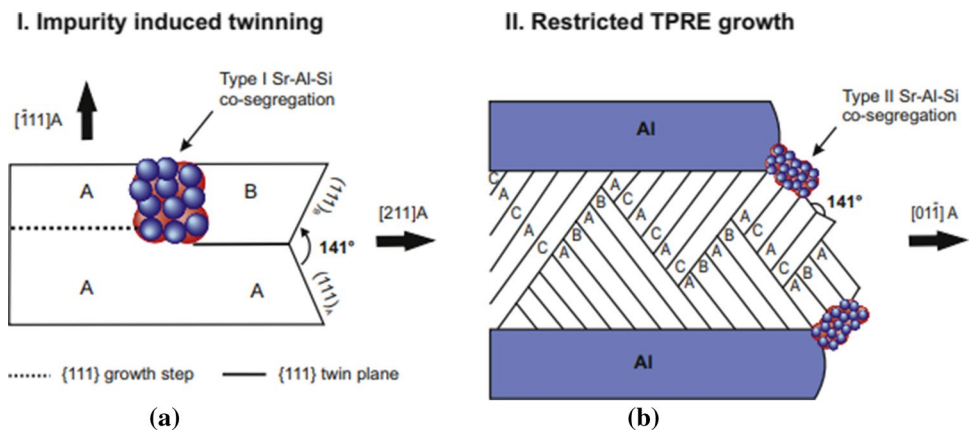


Fig. 15 Undercooling versus interparticle spacing. Reproduced with permission from [108] with permission from Taylor & Francis

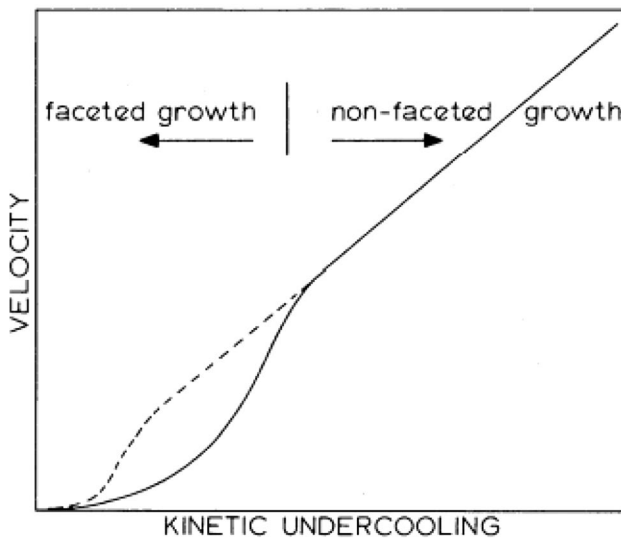


Fig. 16 Undercooling versus growth velocity. The dashed line represents Si in presence of Na and the solid line represents Si in the unmodified alloy. Reproduced with permission from [108] with permission from Taylor & Francis

to be lower as shown in Fig. 44. Hence there must be a balance between these two properties to determine the fatigue life of LCF piston alloys. Figure 44 depicts the particular temperature at which optimum fatigue life can be obtained. Increasing both the intrinsic fatigue toughness, W , at low temperatures and the fatigue cracking exponent, β , at high temperatures, according to the researcher, may be helpful in enhancing LCF life. There is also a critical fatigue test temperature (T_c) between which the highest fatigue life can be determined [75].

Even though the addition of Sr causes an increase in the number of pores that are responsible for crack initiation, it also varies the secondary dendrite arm spacing (SDAS) [12, 92]. Wang et al. [92] examined the heat treatment and eutectic modification influence on secondary dendrite arm spacing (SDAS) and with it the fatigue life of LM25 aluminium alloy. The SDAS was varied by increasing or decreasing the cooling rate. The fatigue life was observed to decrease with a rise in the SDAS value in both finer (SDAS below $60\ \mu\text{m}$) and coarser (SDAS above $60\ \mu\text{m}$) structures in unmodified alloys. In the modified alloy with fine microstructures (SDAS $< 60\ \mu\text{m}$), fatigue life declines with an increase in SDAS values, while in the coarser micrograph (SDAS $> 60\ \mu\text{m}$), fatigue life improves with an increase in SDAS value. Thus it can be concluded that Sr-modified A356 alloy has higher fatigue life compared to unmodified alloy, as shown in Fig. 45. However, the study did not consider the influence of Sr on the increasing porosity of the alloy, which in turn affects the fatigue properties [28]. Hence further research on the impact of Sr on the fatigue life, considering both the parameters (pore formation and fine structure (SDAS value)) is required.

The effect of the amount of eutectic Si on crack propagation mechanisms has been examined by Lados et al. [77] and Kim et al. [128]. The mechanism was studied starting with the near-threshold region to stable crack growth region (Region II) and then to rapid crack propagation region (Region III) [77]. Si contents were varied from no/less Si (1

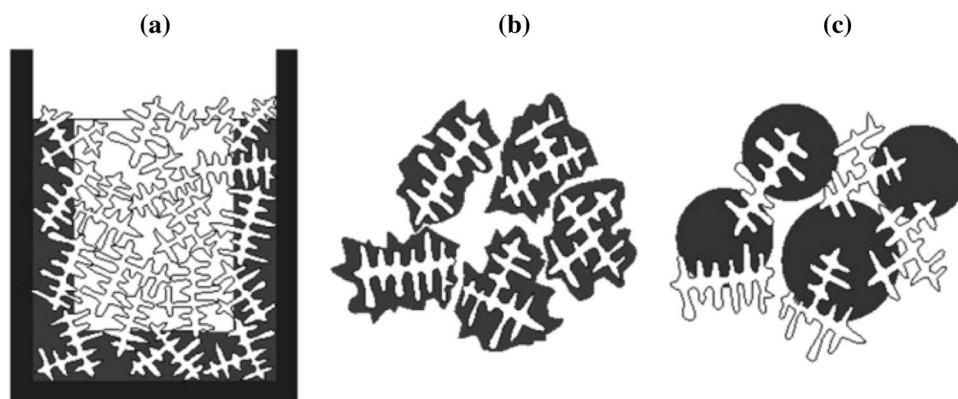


Fig. 17 Nucleation events/modes proposed by Dahle et al. [3] (Reproduced with permission from [3] with permission from the Trans Tech Publications), **a** nucleation at or adjacent to the wall and front growth opposite the thermal gradient, **b** nucleation of eutectic on primary

Aluminium dendrites and, **c** heterogeneous nucleation of eutectic on nucleant particles in the interdendritic liquid (Figure reproduced with permission from [110] with permission from the KOSEF and Australia Academy of Science)

wt%Si) to 7 wt%Si and 13 wt%Si. Fracture toughness was found to be mainly dependent on the morphology of the Si particles. Coarser/unmodified Si microstructure offered convenient pathways for crack propagation, while the modified Si was resistant to crack growth in Region III. The effect of modification was found to be more pronounced in 13 wt%Si

compared to 7 wt%Si. The below figure explains the crack propagation in 7 wt%Si with increasing crack driving force (ΔK). When the value of ΔK is low, the crack contacts with only a few Si particles. At intermediate ΔK values, the crack propagates through a sequence of Si particles mainly located at the cell boundary not too far from the primary crack direction. At high ΔK , the roughness increases, and thus, as the crack is wide enough to destroy more than one Al–Si eutectic, it progresses through the Al–Si eutectic colonies as shown in Fig. 46. The increase in roughness was due to a shift in the crack growth mechanism, from the crack progress through the α -Al matrix to the propagation along/around the eutectic Si.

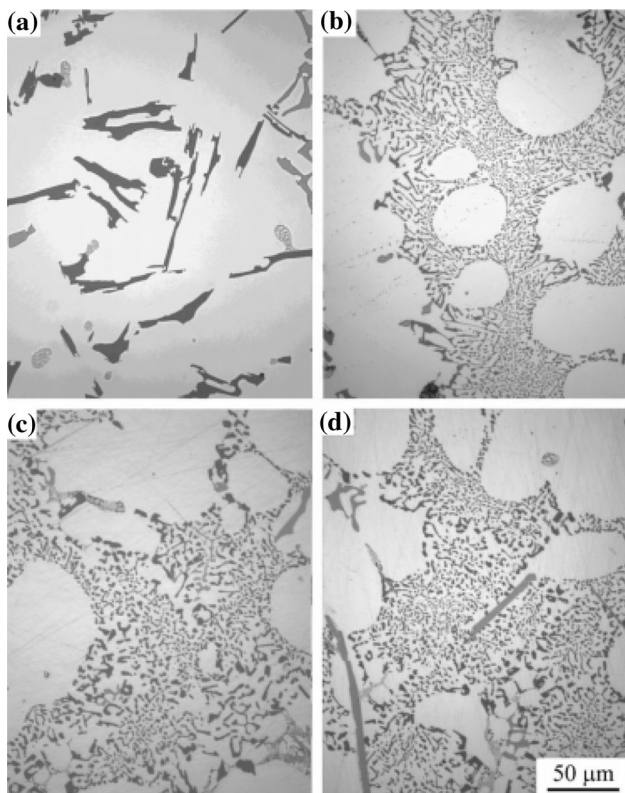


Fig. 18 Microstructures of Al–Si alloys at **a** Unmodified **b** 70 ppm **c** 110 ppm **d** 500 ppm levels. Reproduced with permission from [58] with permission from Springer Nature

Friction stir processing improved fatigue life by breaking the acicular Si fragments within the Al matrix and reducing the casting defects that acted as crack nucleation sites [79, 94]. FSP increased the fatigue life of the formed alloy by 5 times in comparison to the as-cast alloy as can be seen in Fig. 47b. The fatigue life improvement was more pronounced for the stress ratio of $R=0$, wherein the improvement was 15 fold, compared to $R=-1$ stress ratio [78]. Due to grain refinement, friction stirred processed (FSP) alloys were observed to have a higher degree of plasticity induced and roughness induced crack closure. The level of crack closure at $R=-1$ stress ratio, due to the presence of compressive load, was lower than that of the $R=0$ stress ratio which explains its decrease in fatigue life. Nelaturu et al. [93] investigated the occurrence of fatigue cracking at room temperature and growth mechanisms in as-cast and Friction stirred aluminium alloy A356. The friction process combined with the Sr modification resulted in finer grains throughout the microstructure and the Si particles became more uniform and well scattered throughout the aluminium matrix. Crack propagation occurred mainly through the debonding of Si from the Al–Si interface, but in the FSP treated

Fig. 19 Chain of events during eutectic phase nucleation in unmodified Al–Si alloy. Notice the role of β -(Al, Si, Fe) phase in acting as nucleation sites for eutectic Si morphology. Reproduced with permission from [113] with permission from Elsevier

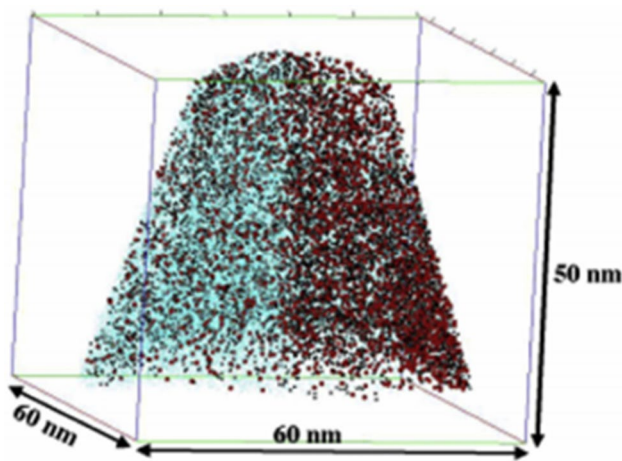
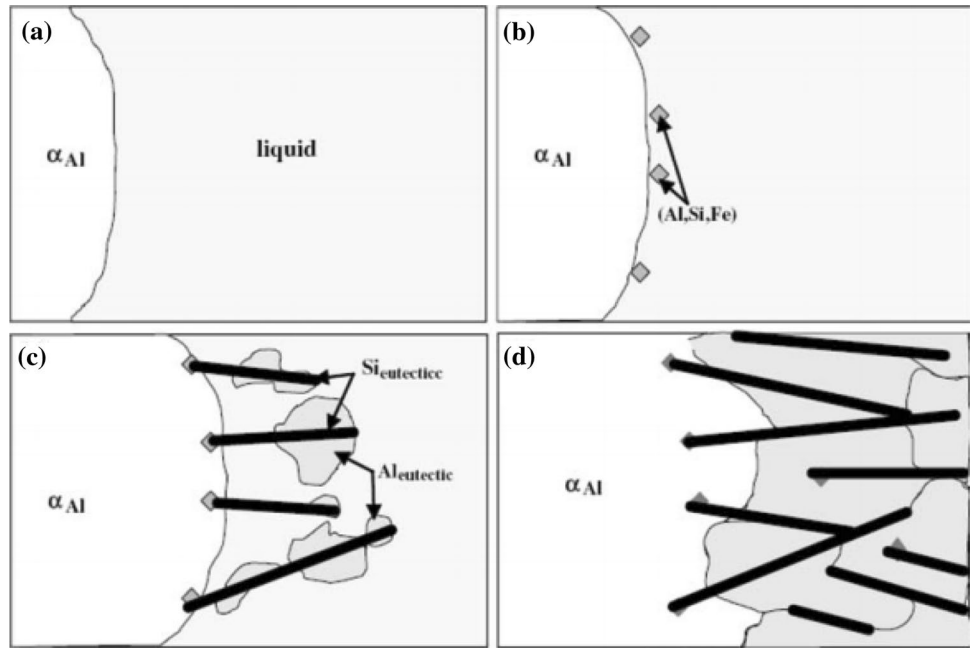


Fig. 20 Sr atoms (marked by red) can be observed in this Atom probe reconstruction image, superimposed on the Si-rich region (marked by black). Reproduced with permission from [14] with permission from Elsevier

samples, the crack had to travel a greater distance through the ductile aluminium matrix before coming across another Si particle. Hence FSP treated samples were found to have superior fatigue resistance compared to as-cast alloys. The fatigue crack initiation was however strictly transgranular at room temperature. An increase by 5 times on FSP treatment was also observed by Nelaturu et al. [76], this time however at an elevated temperature of 150 °C. With an increasing temperature, however, the fatigue crack propagation changed from transgranular to intergranular at higher temperatures. At room temperature, the crack originated at casting defects like pores or laterally persistence slip bands (PSBs), and

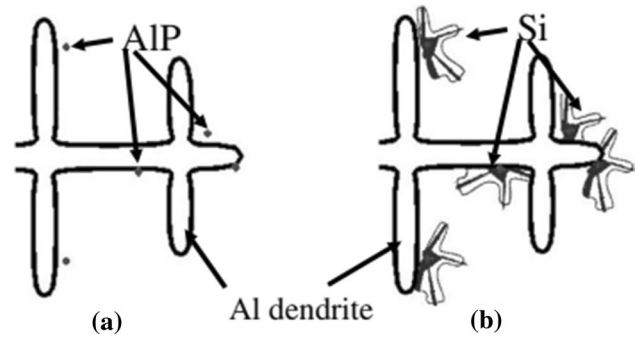


Fig. 21 Influence of AIP as nucleation sites for eutectic Si. Reproduced with permission from [114] with permission from Springer Nature

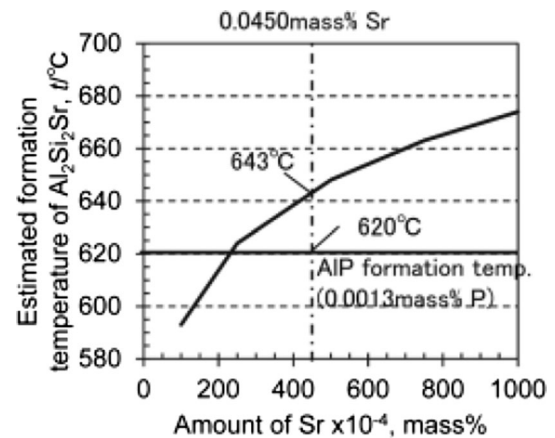


Fig. 22 Estimated formation temperature of Al_2Si_2Sr and AIP. Reproduced from [44] under the terms of the Creative Common License

Fig. 23 Crystal growth model **a** W/o Sr-addition and **b** Sr-addition. Reproduced from [44] under the terms of the Creative Common License

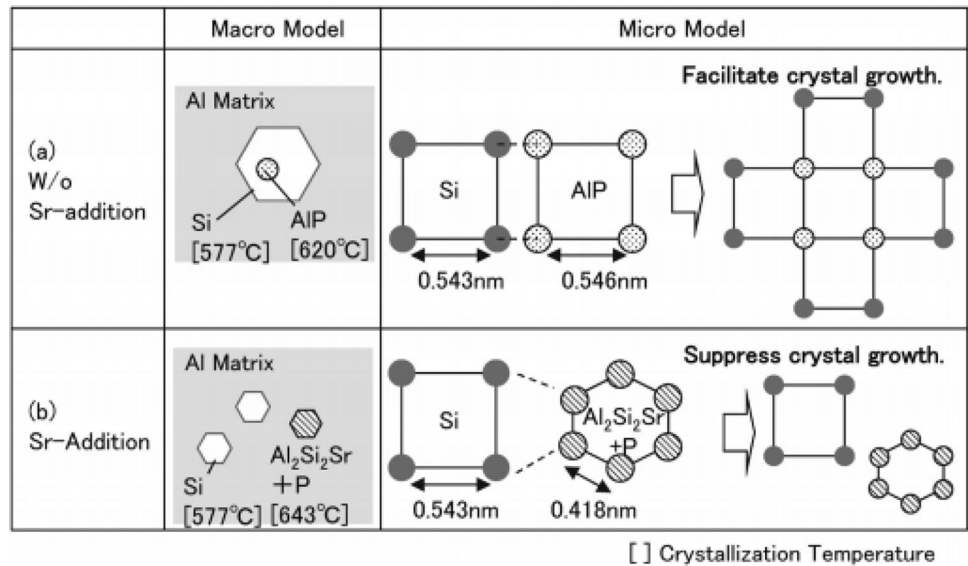


Fig. 24 FE-SEM micrograph of eutectic nuclei in **a** unmodified alloy and, **b** Sr-modified alloy. The arrows depict the direction of faceted growth of eutectic Mg_2Si phase from hexagonal-plate-like Mg_2Si having AIP (Aluminium phosphate) nuclei at its center, Reproduced with permission from [45] with permission from the Trans Tech Publications

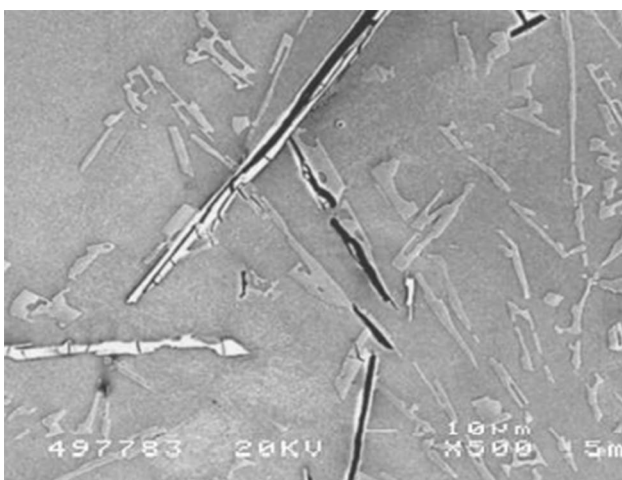
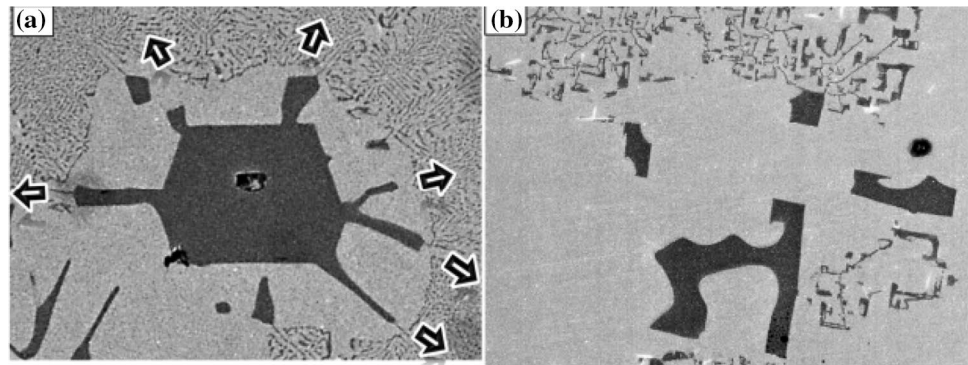


Fig. 25 Bifilms as nucleation sites for β -Fe and eutectic Si particles. Notice the near-perfect crystallographic straightness of the bifilm due to this mechanism. Reproduced with permission from [119] with permission from Springer Nature

grain boundaries were observed to act as a barrier for crack propagation, which is similar to observations of Jana et al. [79]. At higher temperatures, the crack originated along the grain boundaries and a transgranular fracture was observed.

Unlike FSP, other heat treatment processes like T_6 did not affect the fatigue properties. This was observed by Davidson et al. [31] who experimented with the fatigue characteristics of Al-0.6 Mg-7Si alloys which contain trace levels of Sr additions (0.02–0.03 wt%). The standard procedure of heat treatment of these alloys was holding the alloy for 8 h at 540 °C followed by hot-water quench and aging it artificially. It was realized that reducing the solutionising time from 8 to 4 h had no effect on the fatigue endurance properties. Hence a general conclusion can be derived that, precipitation of the Mg_2Si phase which occurs due to the T_6 process only affects the tensile properties of the alloy. The fatigue properties remain more or less unchanged.

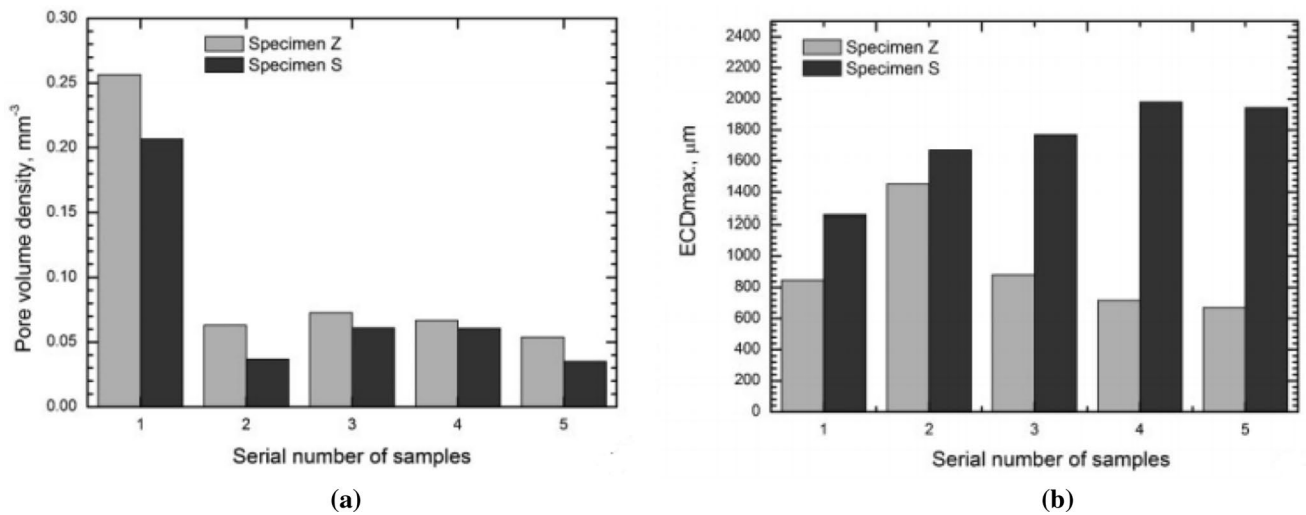
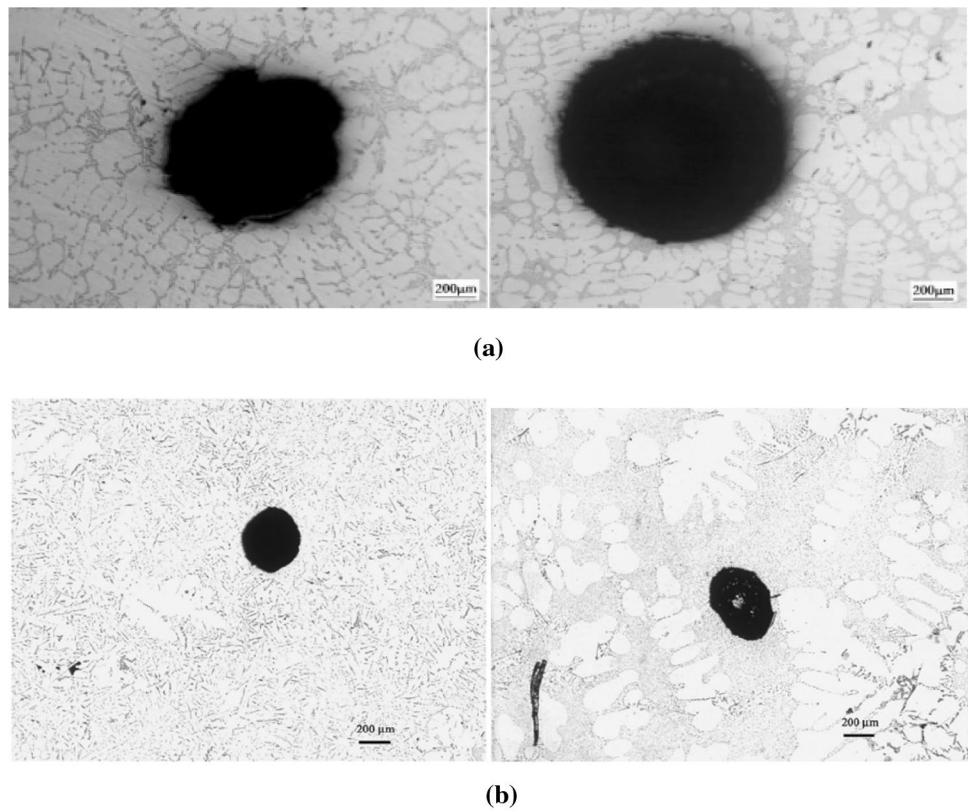


Fig. 26 Bar chart between **a** pore volume density, **b** pore size (Equivalent circle diameter, ECD) along the whole length of specimen Z (unmodified) and specimen S (Sr modified). Reproduced with permission from [24] with permission from Taylor & Francis

Fig. 27 Morphology of large pore observed in unmodified (left) and Sr modified specimen by **a** HC Liao et al. [24] (Reproduced with permission from [24] with permission from the Taylor & Francis), **b** AM Samuel et al. Reproduced with permission from [121] with permission from the Springer Nature



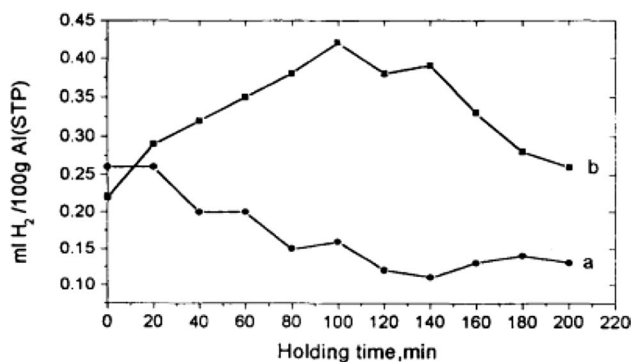
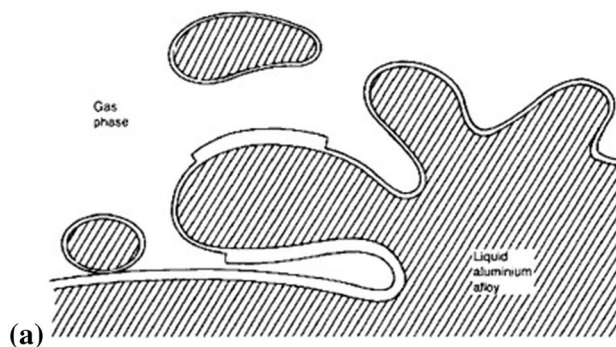


Fig. 28 Hydrogen content vs holding time for **a** unmodified alloy **b** alloy with Sr addition. Reproduced with permission from [23] with permission from Taylor & Francis

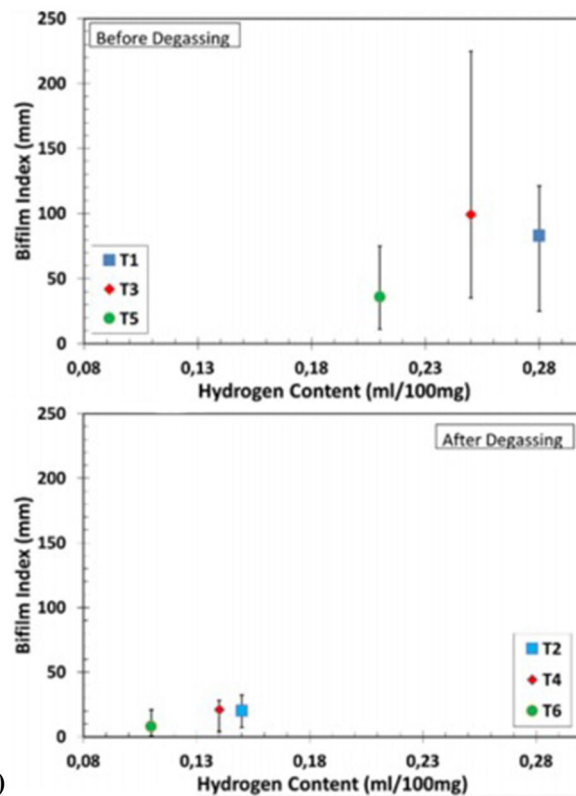
7 Effect of Sr on Corrosion Properties

Aluminium alloys are regularly exposed to an unfavourable environment like rain or seawater and in different liquids in automotive components such as cylinder rings and piston walls. The corrosion characteristics of Al–Si alloys are greatly determined by modifying elements such as Na and Sr. Donald et al. [74] first observed that surface finish deteriorated and the corrosion resistance decreased on adding Sr. On increasing the concentration of Sr, spots on the etched surface of Al–10 wt%Si grew larger as noted in Fig. 48.

Cheng et al. [87] investigated the effect of Sr modification and heat treatment on the corrosion properties of Al–7Si–0.3 Mg in a 3.5wt percent NaCl aqueous solution. The reduction of the size of the eutectic Si particles and the rise in their density have contributed to the appearance of more boundaries of α -Al/Si. These boundaries are most vulnerable to galvanic corrosion, hence the corrosion resistance decreases. Si presents nobler potential compared to Al, and hence in immersing in a corrosive environment, Al is more vulnerable to corrosion, which is called galvanic corrosion. Heat treatment coarsened and reduced the eutectic Si particles density, which reduced the Al/Si boundary and the corrosion susceptibility thereby. It was also found that precipitates also influence corrosion properties, although the quantity of Si particles was greater than that of precipitates produced in A356 alloy, thus greatly reducing its influence. In the unmodified alloy, corrosion spots appeared randomly around the region of the eutectic Si-particle needles as shown in Fig. 49a. Distinguishable pitting corrosion was identified in the interdendritic regions at the vicinity of fibrous eutectic Si particles in the modified A356 alloy as shown by Fig. 49b. In pitting corrosion of Al alloys, chloride ions penetrate the oxide layer either by breaking down the oxide film or by ion migration through vacancies. When a pit is formed at the oxide/metal interface, corrosion develops due to the potential difference between the anodized area inside the



(a)



(b)

Fig. 29 a Bifilm formation due to turbulence as reproduced with permission from [85] with permission from the Taylor & Francis **b** Bifilm index with hydrogen content before and after degassing. Reproduced from [46] under the terms of the Creative Common License

pit and the cathodic area around the pit [89]. Heat treatment changes the microstructure thus decreasing the corrosion damage at the interdendritic region as shown in Fig. 49c. The previous experimental observations of Osorio et al. [88] also suggested that the unmodified together with heat-treated samples having higher corrosion resistance compared to that of modified samples.

The role of oxide layer formation in corrosive growth was investigated by Ozturk et al. [56] and it was observed that, contrary to the previous studies [87, 88], Sr was found to increase the corrosive resistance especially at 120 ppm

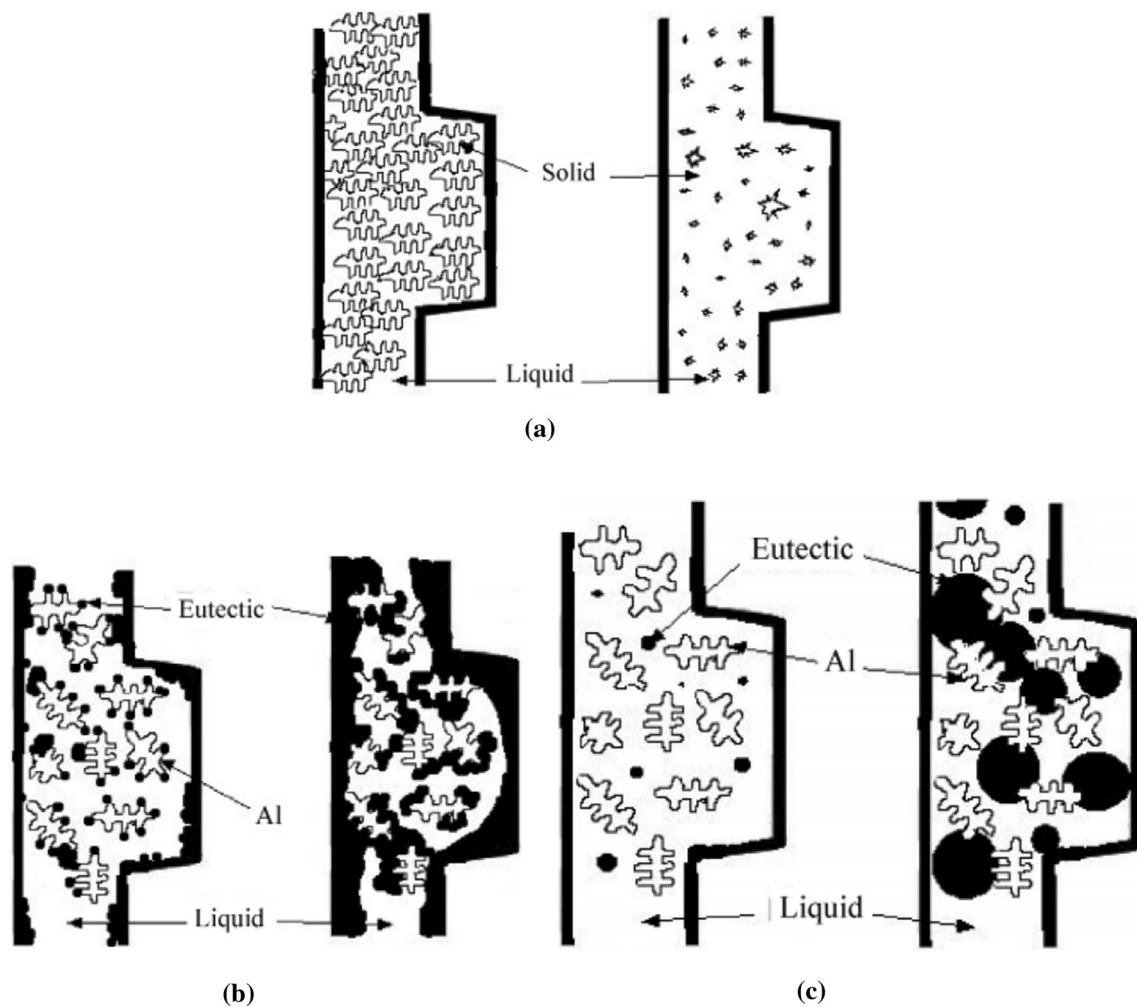


Fig. 30 Illustration of solidification patterns at an early stage and later stage of solidification in **a** Al-1 wt%Si alloy (pure aluminium, Sr free on left and Sr modified on right) **b** Unmodified Al-9 wt%Si alloy,

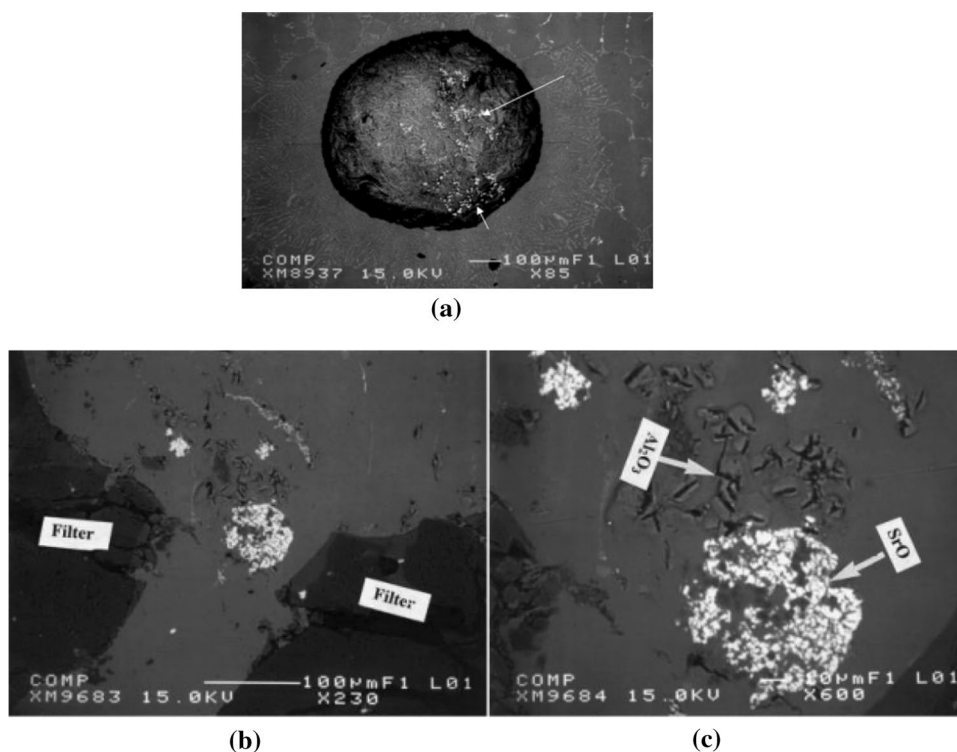
eutectic nucleated at α -Al dendrites, **c** Sr modified Al-9 wt%Si alloy, eutectic nucleated independently in the liquid itself. Reproduced with permission from [83] with permission from Springer Nature

in die-cast A356 alloy and 170 ppm in the sand-cast alloy. Here Potentiodynamic polarization technique was carried out in 3.5 NaCl solution at 1 h immersion time. The corrosion current density i_{cor} at 120 ppm addition in Die-cast alloy was observed to be the lowest of $0.42 \mu\text{Acm}^{-2}$ compared to $13.82 \mu\text{Acm}^{-2}$ (unmodified alloy) which indicated superior corrosion resistance. On increasing the Sr content the i_{cor} value increased again and remain constant. Similarly, in the sand-cast alloys, Sr addition of 170 ppm had the lowest i_{cor} value of $1.47 \mu\text{Acm}^{-2}$. Figure 50 shows the anodic polarization curves of both Die-cast and Sand-Cast alloys. A shift in potential is seen further from that of other alloys indicating superior corrosion resistance. According to the author, the protective layer formation is heavily reliant on the morphology of Si particles. Coarsening of Si particles hinders the formation of these protective oxide layers by forming a heterogeneous structure. The finer Si particles, with the

aid of Sr, form a protective oxide layer in the NaCl solution and improve its corrosion resistance. Figure 51 displays the corroded surfaces of the die and sand casting alloy. It is observed that in the unmodified structures of both die-cast and sand cast alloys, the α -Al dendrites are dissolved and Si remains on the surface like a deep-etched microstructure. On Sr addition, however, the complete dissolution of α -dendrites is no longer observed. This can be attributed to the of Al in a corrosive environment due to Si having nobler potential than Al, as stated by the author.

The above study conducted by Ozturk et al. [56] was only at 1 h immersion time. The effect of immersion time on the unmodified, 50 ppm and 200 ppm Sr modified AlSi9 alloy on its corrosion properties were investigated by Duygun et al. [73]. Sr addition was performed using Al-15%Sr master alloy and the holding time in the furnace was between 4 to 17 h. Three types of alloy were compared; unmodified

Fig. 31 SEM micrographs of A356 alloyed with Sr showing **a** a pore with adequate white Al–Sr–O particles (arrowed). Reproduced with permission from [25] with permission from the Springer Nature, **b** Al_2SrO_3 particles passing through pores of the filter at lower magnification and, **c** on further magnification. Reproduced with permission from [40] with permission from the Taylor & Francis



base alloy (AD1), 50 ppm Sr alloy (AD2) obtained at 17 h holding time, and 200 ppm Sr alloy (AD3) obtained at 4 h holding time. The lower concentration of Sr in the second alloy is attributed to the disappearance of Sr from liquid alloy when held at 17 h in the furnace. Potentiodynamic polarization technique was conducted at various immersion times in 3.5 wt% NaCl solution to understand the corrosive behaviour. It was observed through potentiodynamic polarization curves, the corrosion current density (i_{cor}) values increased with an increase in immersion time and corrosion potential, (E_{corr}) shifted in the negative direction, irrespective of Sr content, indicating the rapid increase in corrosion rate in the alloy. As shown in Fig. 52, the highest charge transfer resistance values (R_{ct}), which indicate greater corrosion resistance of the alloy, are the highest in the case of 1 h holding time for all test samples. It can also be seen that the i_{cor} and R_{ct} values are more stable for 200 ppm Sr alloy indicating that an increase in eutectic phase in the alloy formed more stable oxide layers which increased its corrosion resistance. The 50 ppm Sr content in AD2 alloy however did not affect its corrosion properties significantly due to few amount of protective oxide layer formation. The decrease in R_{ct} indicated the degradation of the protective oxide layer which promotes the corrosion resistance and pit formation in the alloy.

8 Wear Properties of Sr Modified Alloys

The wear rate was considerably decreased by Sr additions. The wear resistance was found to be least in unmodified alloys due to the plate/needle-like Si particles which acted as stress elevators [10, 11, 34, 129–131]. The finer the morphology of the particles, the dislocations due to external force are easily transmitted, hence the more resistance to fracture or deformation. The unmodified needle-shaped Si particles have a greater tendency for micro-cracks formation increasing their wear rate. Squeeze casting of the alloys was found to produce a much finer microstructure compared to gravity casting [10]. Hence squeeze cast alloys having a much lower wear rate than gravity cast alloys. The worn-out surfaces of unmodified, Sr modified, and Sr modified squeeze cast alloys were compared and it was observed that the adhesive wear was observed in unmodified alloys, in the form of infringement of micro-weld in the slide surface. These micro-welds were less detected in the alloy modified by Sr and the abrasion-related grooves and strips totally disappear in the Sr modified Squeeze cast alloy. Lee et al. [87] examined the wear-corrosion characteristics of Sr modified alloy and the influence of heat treatment process on the properties, in 3.5 wt% of NaCl aqueous solution. It has been observed that in the Sr modified alloys, while wear

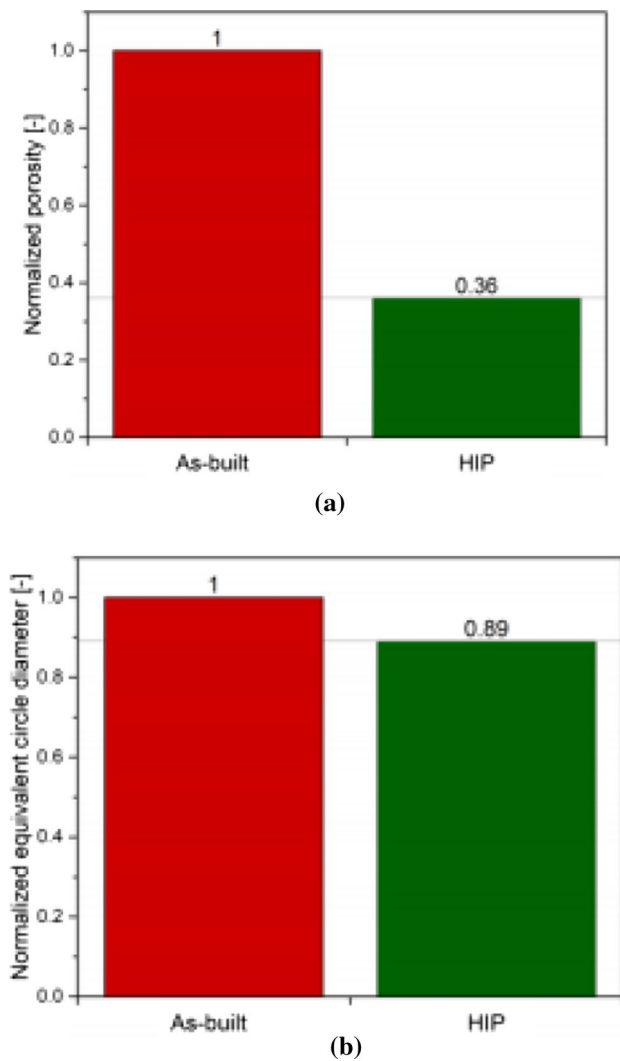


Fig. 32 Effect of HIP treatment on **a** porosity **b** pore diameter. Reproduced from [30] under the terms of the Creative Common License

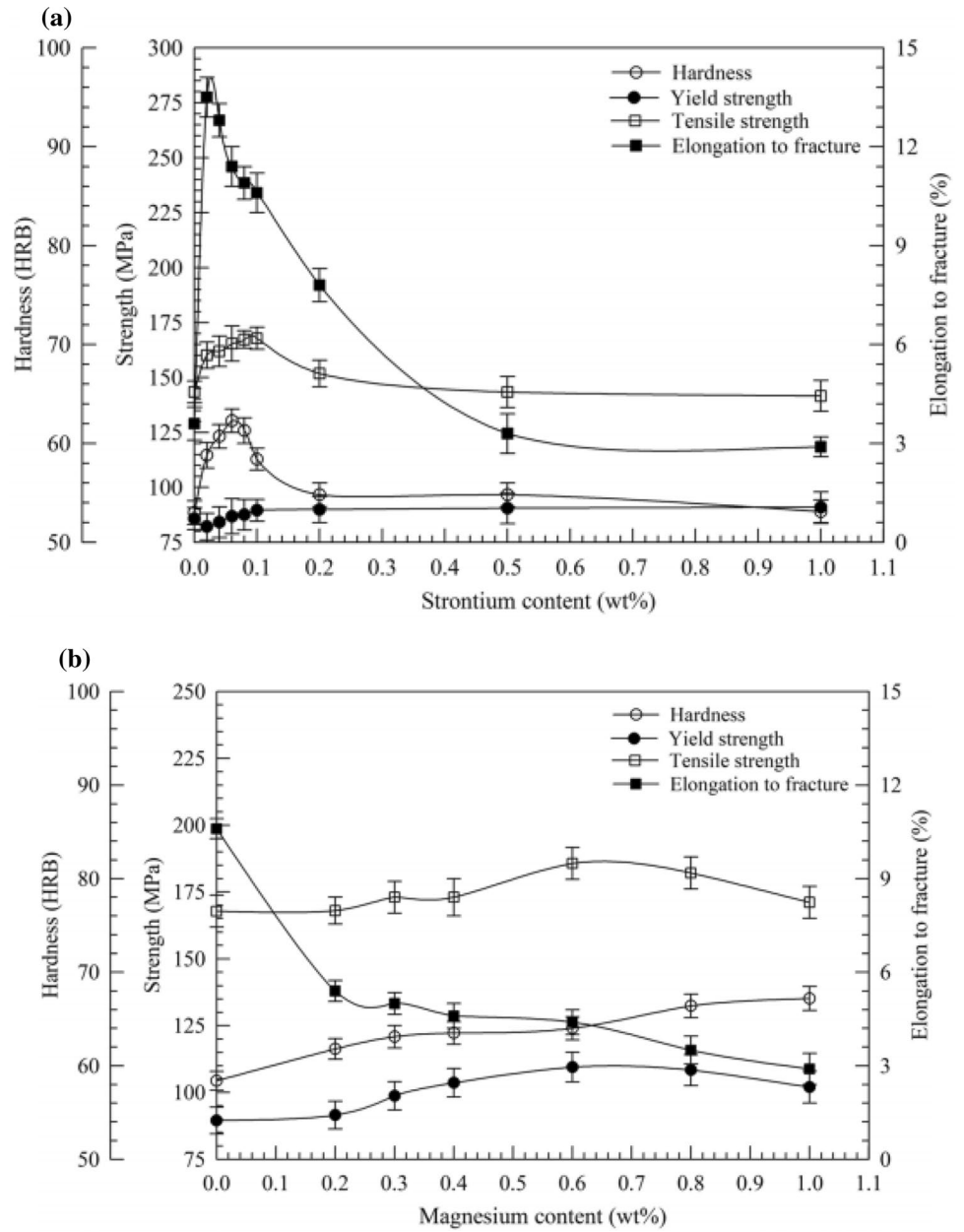
resistance has improved, the corrosion susceptibility to the eutectic Al/Si boundary balances this effect, leading to an overall marginal improvement in the wear-corrosion rate compared to unmodified alloys. Heat treatment was found to decrease the wear-corrosion rate, as shown in Fig. 54, with modified-T6 Al–Si–Mg alloy having the least wear-corrosion rate compared to T7 and T4 treatments. The decrease in wear-corrosion rate due to heat treatment was attributed to the surge in the wear resistance and decrease in corrosion susceptibility at the eutectic region. As the wear tests proceeded, oxide films formed at the site of wear, increasing its wear resistance and avoiding any further damage to the surface of the alloy as shown in Fig. 53.

9 Summary

The outcome of Sr modified Al–Si binary alloy and Al–Si–Mg alloy was studied in detail and the key conclusions are summarized as follows:

- The different ternary phases formed on Sr modification were described by many researchers and they were: AlSiSr , $\text{Al}_2\text{Si}_2\text{Sr}$, $\text{Al}_2\text{Si}_2\text{Sr}_3$, $\text{Al}_{16}\text{Si}_{30}\text{Sr}_8$, $\text{Al}_2\text{Si}_3\text{Sr}_3$, $\text{Al}_2\text{Si}_4\text{Sr}_3$, $\text{Al}_2\text{Si}_7\text{Sr}_5$, $\text{Al}_3\text{Si}_7\text{Sr}_{10}$, $\text{Al}_6\text{Si}_3\text{Sr}_{20}$, $\text{Al}_6\text{Si}_9\text{Sr}_{10}$, $\text{Al}_8\text{Si}_3\text{Sr}_{14}$, and AlSi_6Sr_4 . Of them, the formation enthalpies of all the 10 phases except $\text{Al}_6\text{Si}_9\text{Sr}_{10}$ and AlSi_6Sr_4 were found to be negative indicating its formation at the ground state of the system at room temperature. The most important intermetallic compounds are AlSiSr and $\text{Al}_2\text{Si}_2\text{Sr}$, and most of the studies have investigated in-depth these two ternary phases.
- CALPHAD (Calculation of Phase Diagram) method was utilized to compute the thermodynamic properties and phase equilibria of AlSiSr and $\text{Al}_2\text{Si}_2\text{Sr}$ ternary phases. However, the thermodynamics of the other 10 phases should be studied in detail. The phase diagram and isothermal section of the Al–Si–Sr ternary system constructed by the researchers reveal to us a lot about the different reactions and their corresponding temperatures.
- Sr changes the morphology of Si from the coarse plate-like to fine fibrous structure. Although the main cause for this modification is still debated among researchers, two theories have surfaced, providing the most probable explanation to this phenomenon: (1) Restricted growth theory and, (2) Restricted nucleation theory.
- Unmodified silicon structure is seen to have slight or no twins, however, Sr alteration increases the twin density. According to the restricted growth theories, strontium is adsorbed by silicon liquid front, preventing the attachment of silicon atoms to the crystal and thereby promoted multiple twinning and hence the fibrous structure. Whereas due to some discrepancies in this theory, restricted nucleation theory have surfaced which states that alloying of Sr delays the clustering tendencies of silicon atoms near temperatures at the nucleation event, and thus the morphology changes.
- Sr addition also causes modification in the Mg_2Si phase in ternary Al–Si–Mg alloys, the most notable being the change from fragmented phase to skeletal. Other changes include in eutectic nucleation mode from heterogeneous to homogenous, and upon solidification, the restraining effect on the crystallization of the Mg_2Si phase occurs. High Mg addition was also found to mask the effect of Sr modifications due to the formation of Mg–Sr intermetallic compounds.

Fig. 33 The change in hardness and tensile characteristics to fracture of **a** Al–Si alloy with change in Sr content and **b** Al–Si–Mg alloy with variation in Mg content. Reproduced with permission from [49] with permission from Springer Nature



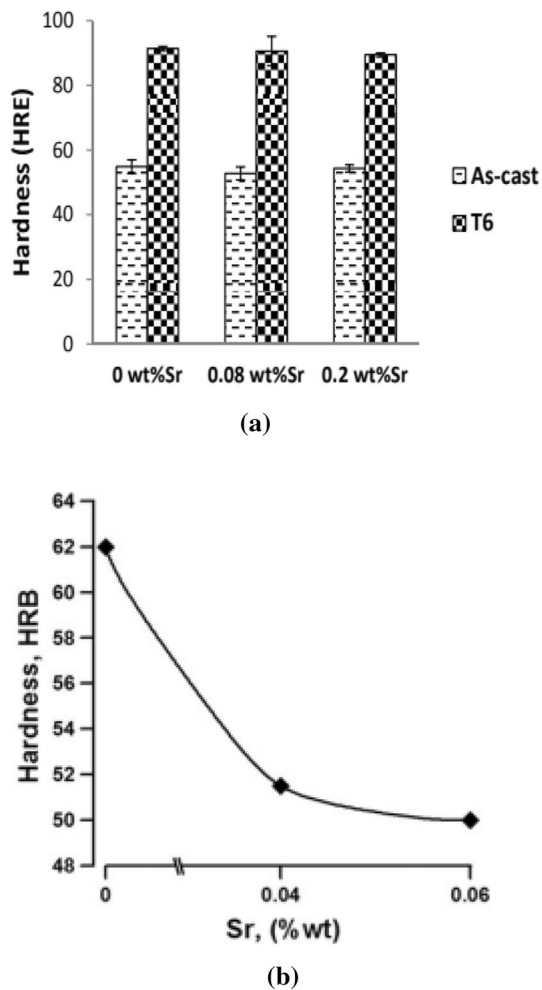


Fig. 34 The value of hardness for **a** Sr content and T6 treatment as calculated by Sangchan et al. [3] (Reproduced with permission from [3] with permission from the Trans Tech Publications.) and, **b** Sr content as calculated by Rodriguez et al. [66]. (Reproduced with permission from [66] with permission from the Elsevier)

- Porosity increase in the alloy is observed by many researchers on Sr addition. However similar to the previous reason for morphology change in Si, this phenomenon remains under discussion among researchers. Many researchers claim that Sr addition:
- Increases the formation of Strontium related oxides and hence these act as nucleation sites for pore formation.

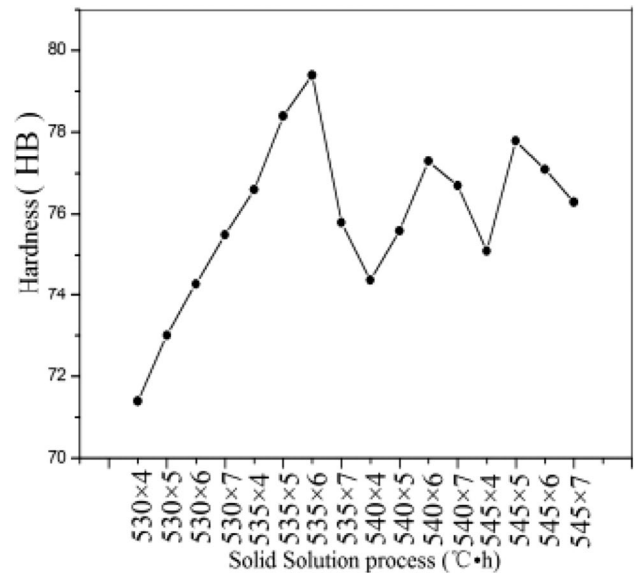


Fig. 35 Comparison of hardness under different solution temperature and holding times. Reproduced with permission from [6] with permission from the Trans Tech Publications

- Reduces the surface tension between the pore and the liquid, which is responsible for the growth of the pore.
- Increases the hydrogen content in the melt causing early hydrogen bubble formation and thus creating pores after solidification. Many authors suggested degassing techniques like rotary degassing to remove such gases.
- Increases the Bifilm index, which increases bifilm at the surface of the melt causing pores at the cast surfaces.
- Lowers of eutectic temperature, resulting in more time for the growth of pores.
- Change in eutectic nucleation mode i.e., eutectic grain nucleates in the liquid independently in Sr added alloy rather than at the edge of α -Al dendrites.
- The influence of Strontium on the mechanical properties, according to different researchers, was reviewed in detail. The behaviour of properties like hardness, tensile strength, yield strength, ductility, impact toughness, and fatigue heavily depended on Sr content and the heat treatment process and variables used.
- Considerable change in hardness was not observed by increasing the Sr content when compared to modification

Fig. 36 Spherodisation of Si on solution treatment. Reproduced with permission from [7] with permission from the Elsevier

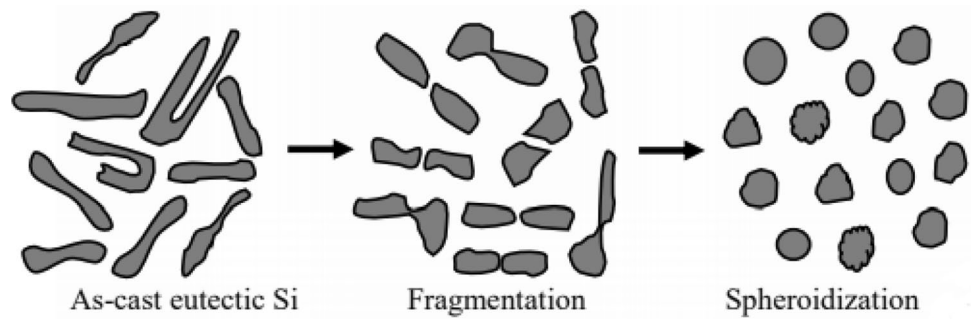


Fig. 37 Si morphologies versus mechanical properties of HPDC A383 alloys. Reproduced with permission from [29] with permission from Elsevier

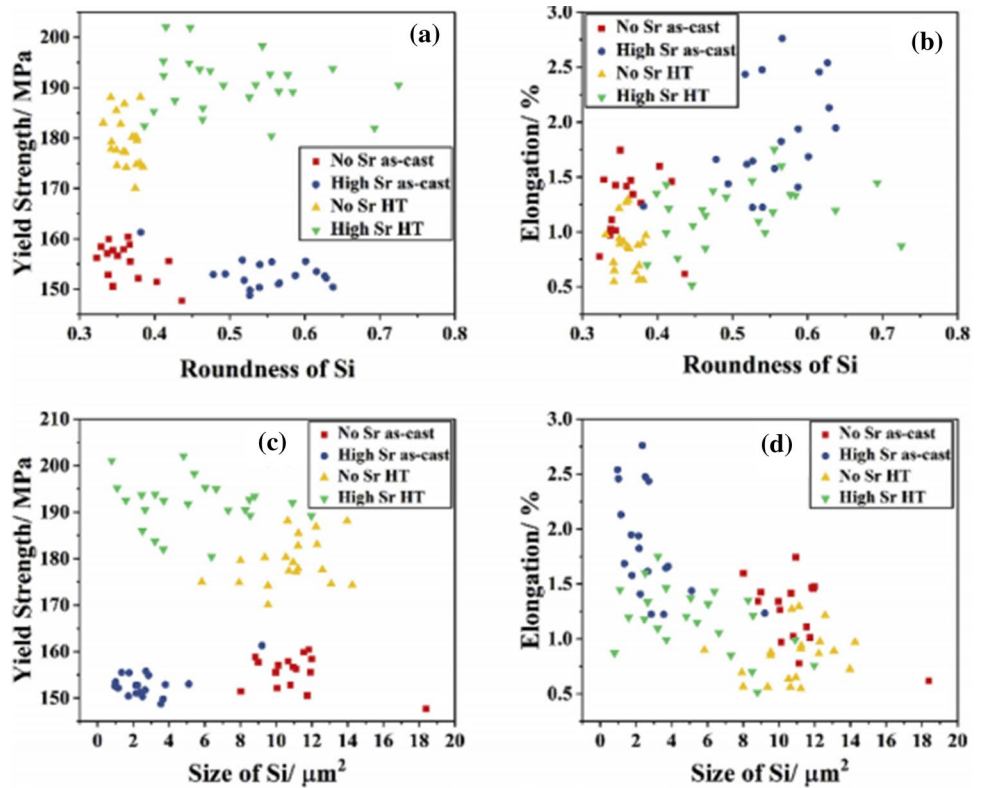
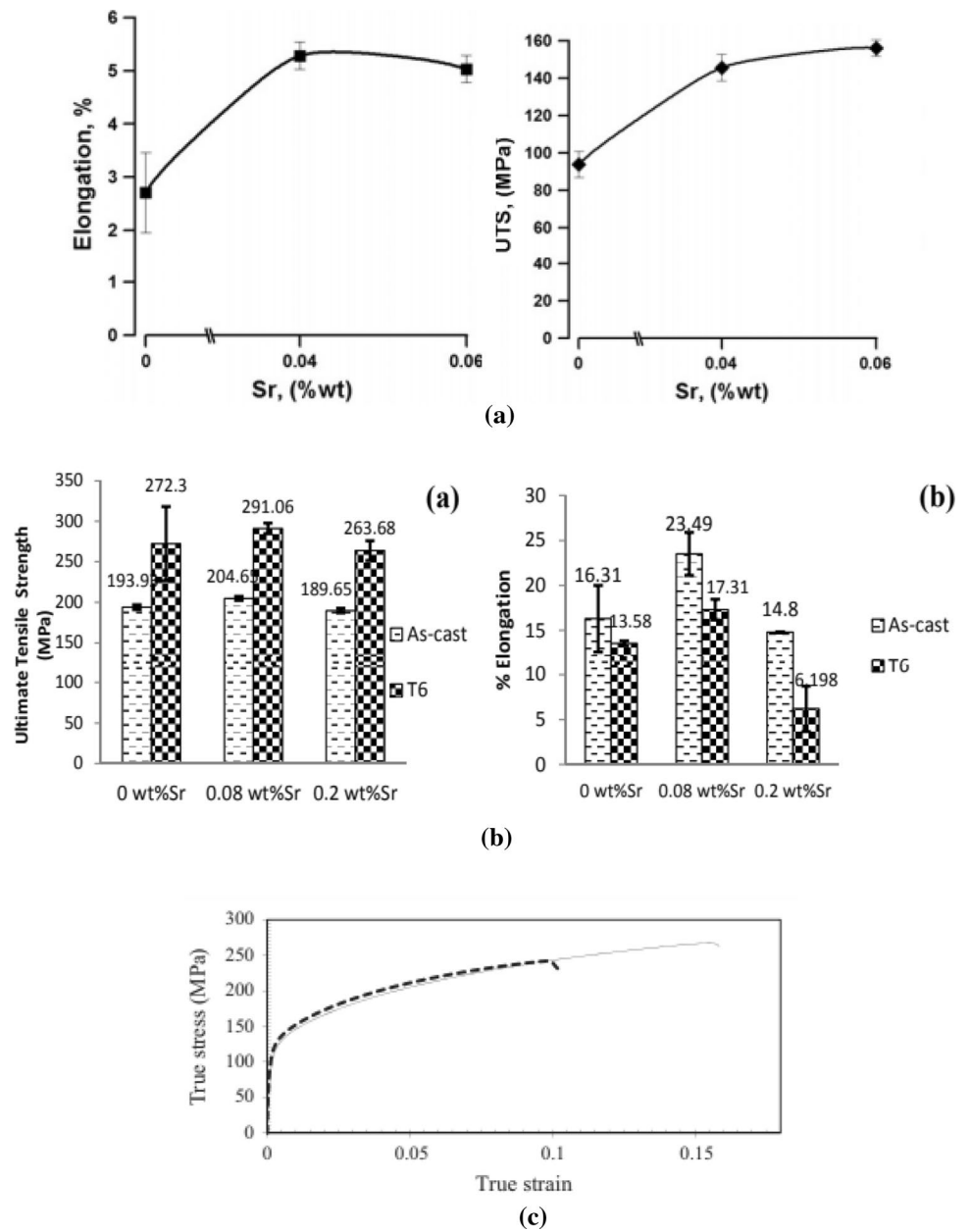


Fig. 38 Variation in mechanical properties according to different studies **a** S Haro-Rodriguez et al. [66] (Reproduced with permission from [66] with permission from the Elsevier), **b** Sangchan et al. [3] (Reproduced with permission from [3] with permission from the Trans Tech Publications) (c) Stress–strain curves of unalloyed (dashed line) and Sr-alloyed (solid line) A356 alloy (Reproduced with permission from [48] with permission from the Elsevier)



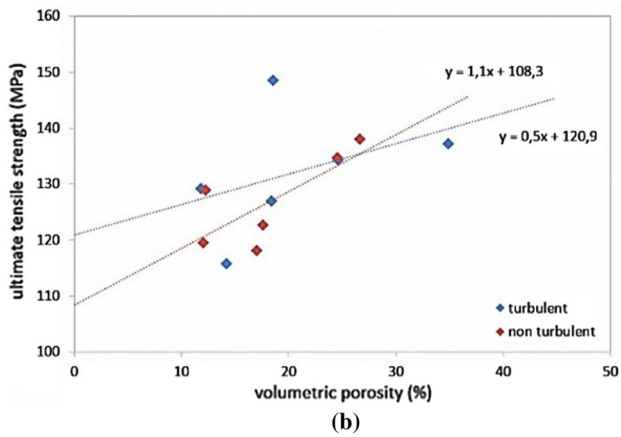
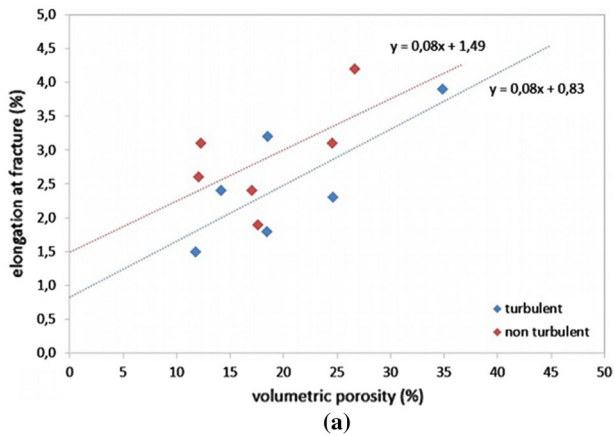


Fig.39 Variation in mechanical properties by porosity **a** elongation **b** ultimate tensile strength (UTS) Reproduced from [64] under the terms of the Creative Common License

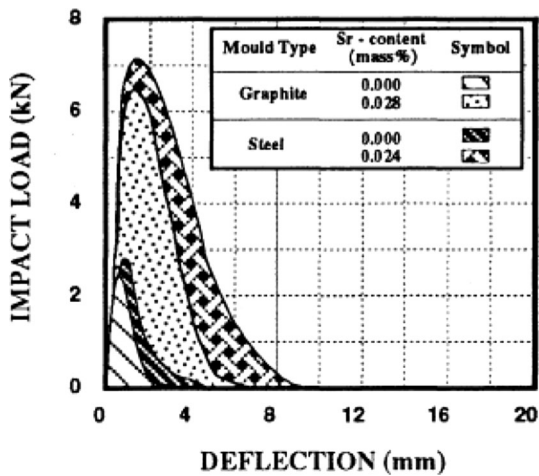


Fig.40 Typical load–deflection curves for samples of non-modified and modified alloys. Reproduced from [90] under the terms of the Creative Common License

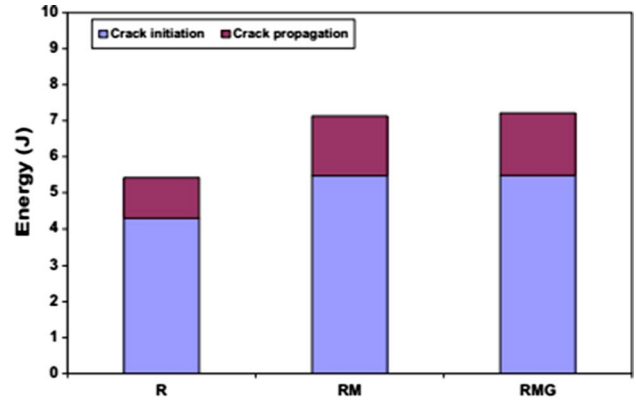


Fig.41 Impact energy in the as-cast samples. Here R represents as-cast alloy, Rm is the Sr altered alloy, and RMG is the Sr modified and grain refined alloy. Reproduced with permission from [62] with permission from Elsevier

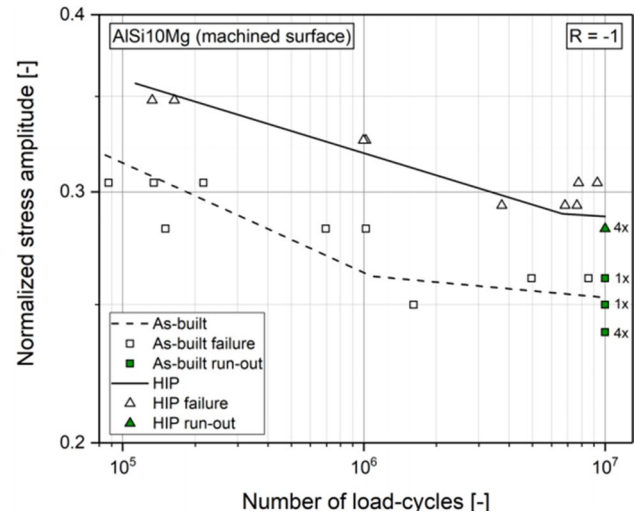


Fig.42 S–N curves for as-built and HIP treated AISi10Mg alloy. Reproduced from [30] under the terms of the Creative Common License

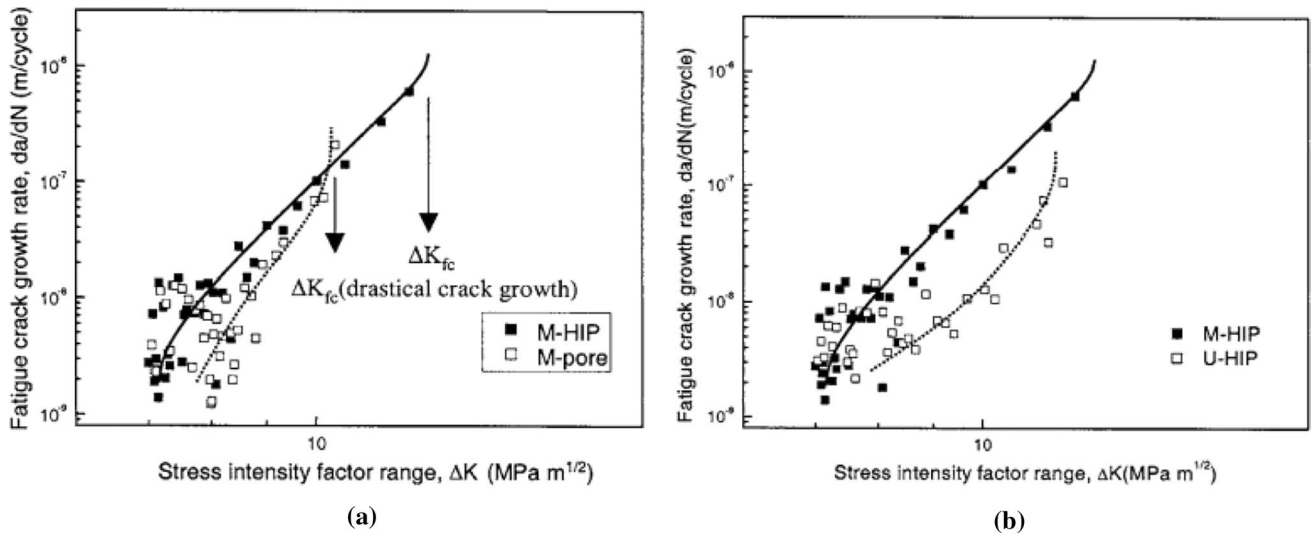


Fig. 43 Fatigue crack growth rate (da/dN) versus stress intensity factor range (ΔK) for **a** M-HIP (modified HIP) and M-pore (modified no HIP), **b** M-HIP (modified HIP) and U-HIP (unmodified HIP). Reproduced with permission from [80] with permission from Springer Nature

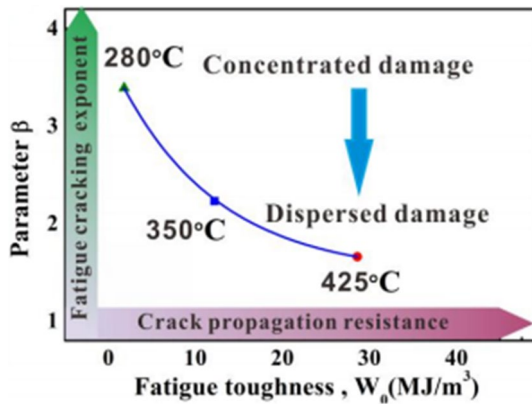


Fig. 44 The relation between damage mechanism and fatigue parameter. Reproduced with permission from [127] with permission from Elsevier

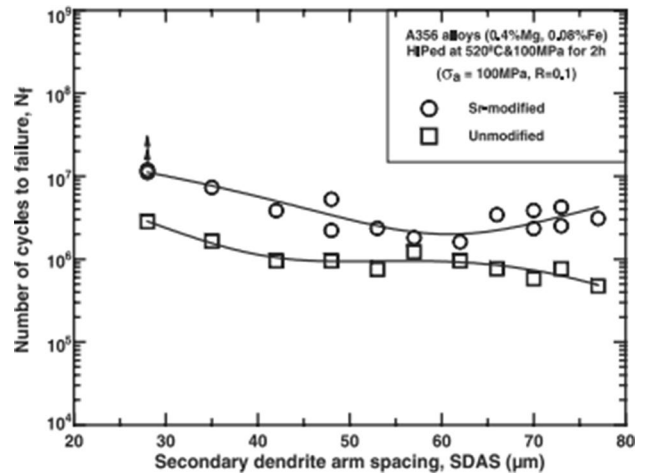


Fig. 45 Fatigue life for unmodified and Sr modified A356-T6 alloy concerning SDAS. Reproduced with permission from [92] with permission from Elsevier

Fig. 46 Crack morphology and propagation in 7 wt% Si alloy for various ΔK levels. Reproduced with permission from [77] with permission from Elsevier

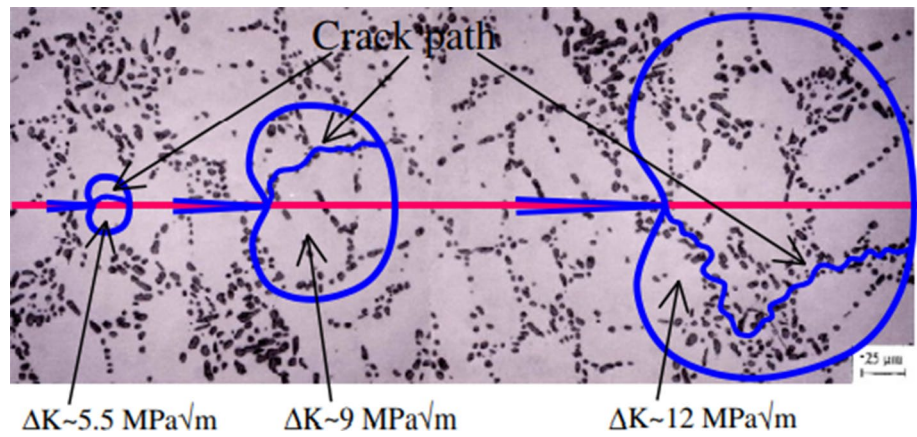


Fig. 47 Fatigue properties of the cast and S–N plot for FSP a Cast (right side) and FSP (left). Reproduced with permission from [79] with permission from Elsevier

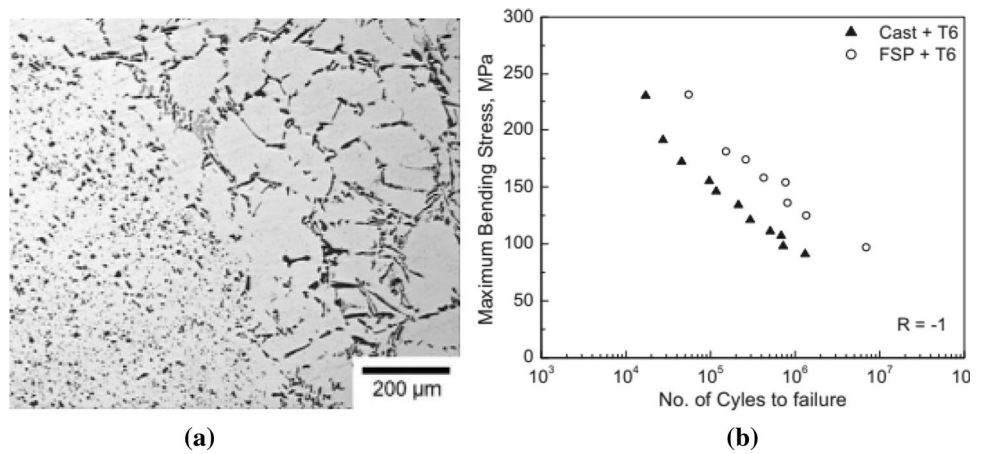


Fig. 48 The surface finish of Al–Si castings with increasing Sr additions from 0 to 150 ppm. One can notice an increase in size and number of Spots. Reproduced from [74] under the terms of the Creative Common License

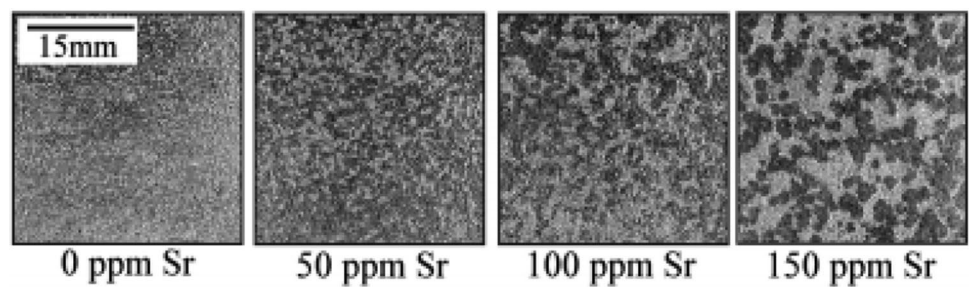
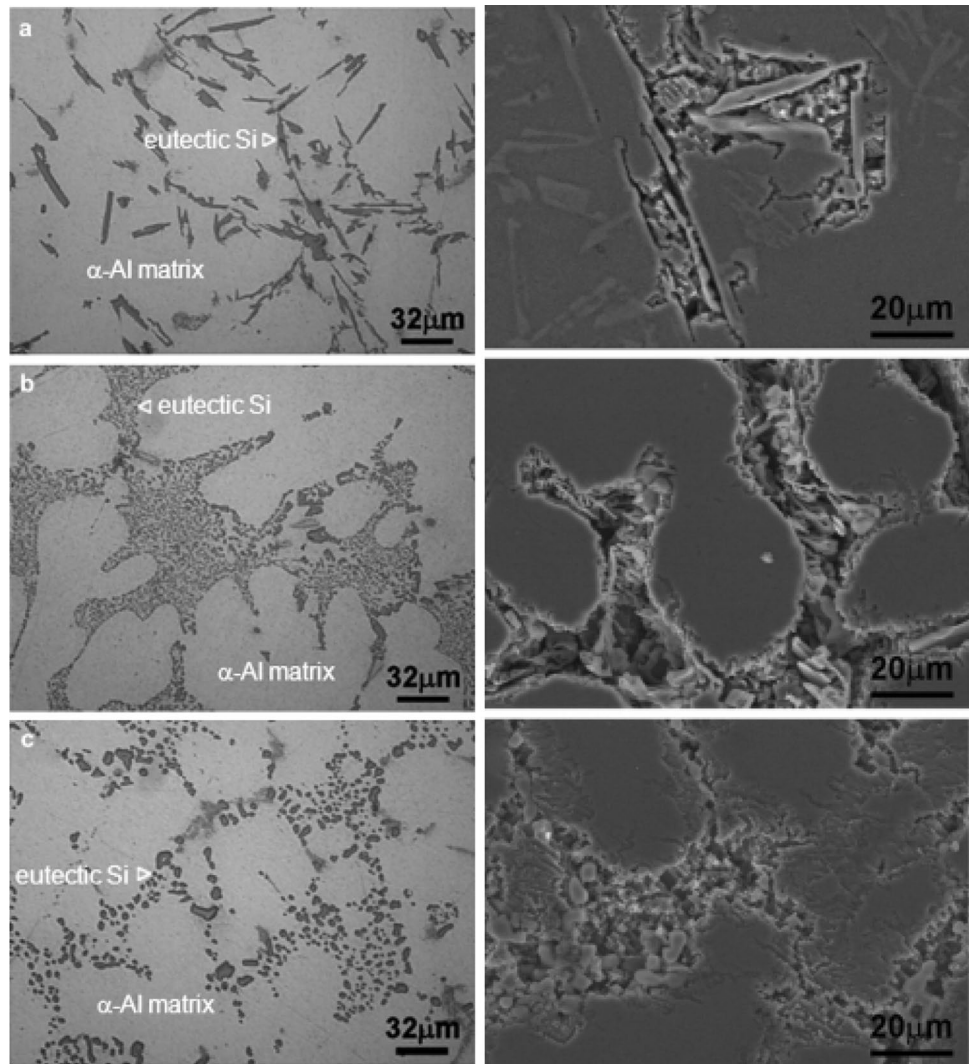


Fig. 49 Before (left) and after corrosion surfaces of **a** unmodified **b** Sr modified **c** T6 heat-treated A356 alloy. Reproduced with permission from [87] with permission from Elsevier



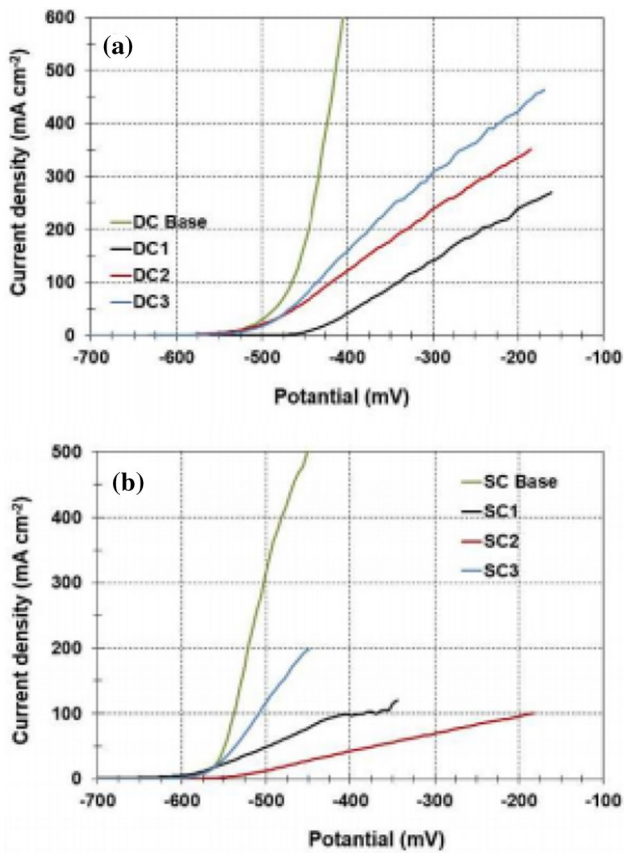


Fig. 50 Anodic polarization curves for alloys **a** Die cast, DC Base (unmodified), DC1 (120 ppm Sr), DC2, DC3 (> 120 ppm Sr) **b** Sand cast, SC base (unmodified), SC1 (120 ppm Sr), SC2 (170 ppm Sr), SC3 (> 170 ppm Sr). Reproduced with permission from [56] with permission from the Elsevier

by heat treatment. T6 treatment especially was advised by many researchers for the increase in hardness.

- Sr modification cause a change in Si morphology from needle shape to a more fibrous structure, and hence reduces higher stress concentration influence at the

sharp corners of the Si needles. Hence, Sr modified alloy experience a considerable improvement in their tensile strength, ductility, and elongation properties.

- Yield strength, however, shows no increase or decrease on Sr addition. Rather it was observed that Mg content has a much higher impact on the yield strength
- Holding time in the solution treatment process is observed to be avital factor in determining the properties of the alloy. Other treatment processes like T6 and melt treatment were also applied by the researchers.
- The impact toughness of Al–Si alloys is dependent on the microstructure which is heavily dependent on the content of the Sr modifier, melt treatment processes, and the solidification conditions.
- Since the Al–Si piston alloy is frequently subjected to fatigue loading, the effect of Sr content and heat treatment processes was studied.

However, corrosion resistance was found to deteriorate on increasing Sr contents. Many researchers suggest that the unmodified and heat-treated samples possess higher corrosion resistance than Sr modified samples. The decline in the size of eutectic Si particles and surge in its density, on Sr addition, caused more boundaries of α -Al/Si to appear. These boundaries were most vulnerable to galvanic corrosion, hence the corrosion resistance decreases

The wear properties showed improvement on Sr additions. Many researchers observed an increase in the wear resistance in Sr modified alloys. The unmodified needle-shaped Si particles have a greater tendency for micro-cracks formation increasing their wear rate. The finer the morphology of the elements in Sr altered alloys, the dislocations due to external force are easily transmitted, hence the more resistance to fracture or deformation.

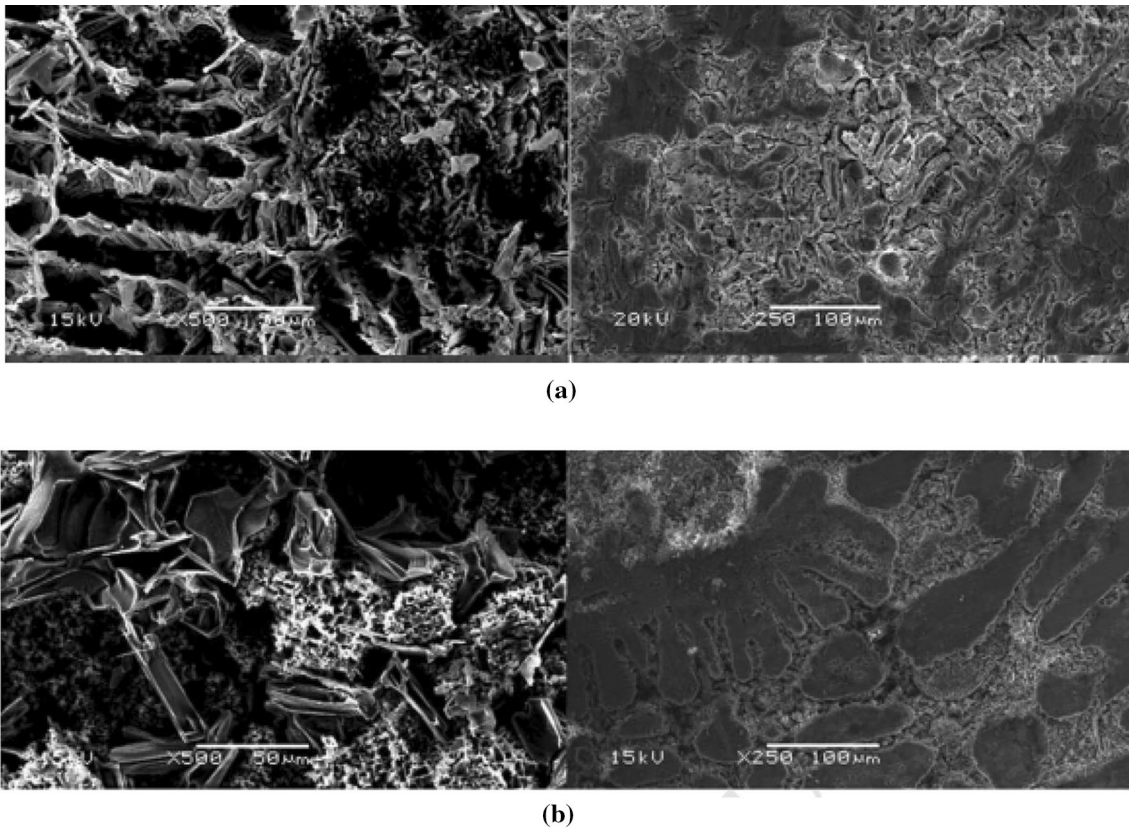
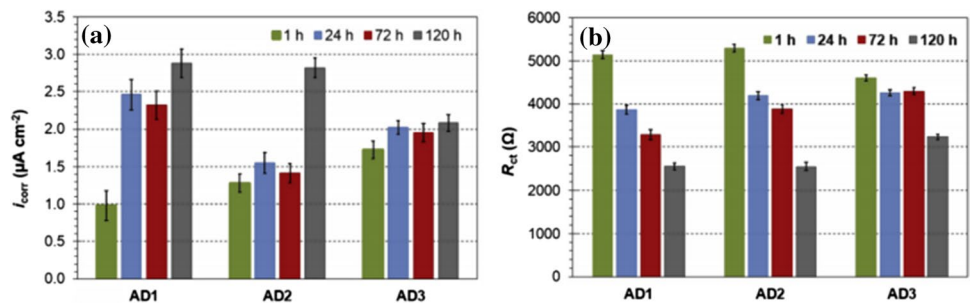


Fig. 51 SEM images of corroded surfaces of **a** unmodified and modified die-cast Al-Si alloy **b** unmodified and modified sand-cast Al-Si alloy. Reproduced with permission from [56] with permission from Elsevier

Fig. 52 The current density change (i_{cor}) and transfer resistance (R_{ct}) of the alloy at various immersion times. Reproduced with permission from [73] with permission from Elsevier



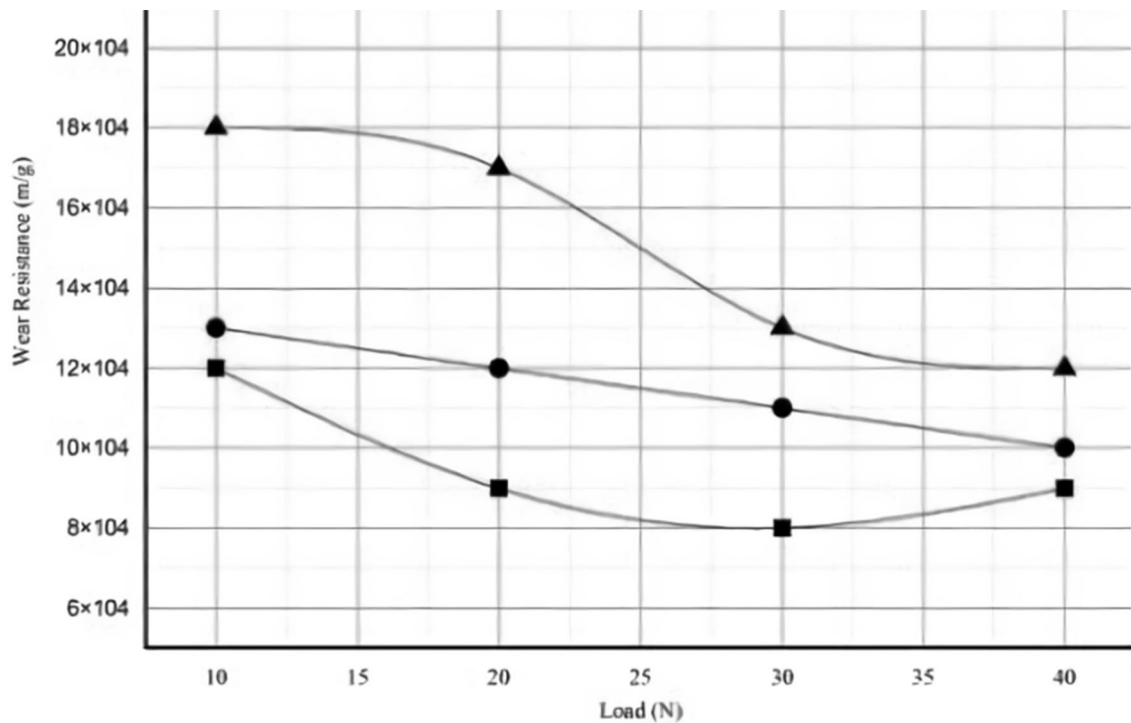


Fig. 53 Wear behaviour of Al₁₂Si₃Cu₁Mg_{1.7}Ni alloy of unmodified gravity casting (Δ), Sr modified gravity die-cast (○), Sr modified + squeeze cast (□). Reproduced with permission from [10] with permission from Taylor & Francis

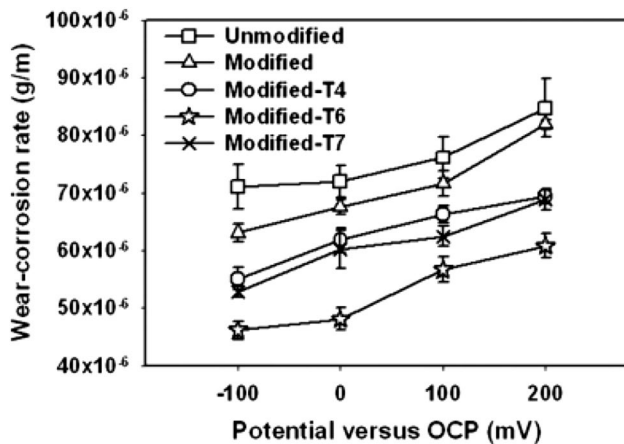


Fig. 54 Unmodified and modified wear- corrosion rate of A356 alloys in various tempered. Reproduced with permission from [87] with permission from Elsevier

References

1. V.V. Ramalingam, P. Ramasamy, M.D. Kovukkal, G. Myilsamy, *Met. Mater. Int.* **26**, 409 (2020)
2. S. Derin, Y. Birol, U. Aybarc, *Int. J. Metalcast.* **11**, 688 (2017)
3. A. Sangchan, T. Plookphol, J. Wannasin, S. Wisutmethangoon, *Adv. Mater. Res.* **893**, 353 (2014)
4. B. Li, Z. Zhang, Z. Wang, M. Tang, Z. Wei, J. Xu, *Spe. Cast. Nonferrous Alloys* **33**, 691 (2013)
5. D. Wang, H. Zhang, X. Han, B. Shao, L. Li, J. Cui, *J. Mater. Eng. Perform.* **26**, 4415 (2017)
6. J.X. Lin, J.P. Zhang, L.Y. Niu, D.R. Sun, Z.M. Shi, Y. Li, G.Y. Li, *Mater. Sci. Forum* **749**, 1 (2013)
7. Y.C. Lin, S.C. Luo, J. Huang, L.X. Yin, X.Y. Jiang, *Mater. Sci. Eng. A* **725**, 530 (2018)
8. M. Uludağ, L. Gemi, D. Dişpinar, *Int. J. Sci. Tech. Res. Eng.* **1**, 21 (2013)
9. A.M. Samuel, G.H. Garza-Elizondo, H.W. Doty, F.H. Samuel, *Mater. Des.* **80**, 99 (2015)

10. K. Pratheesh, M. Ravi, A. Kanjirathinkal, M.A. Joseph, *Int. J. Cast Metal. Res.* **28**, 301 (2015)
11. C.Y. Yang, S.L. Lee, C.K. Lee, J.C. Lin, *Wear* **261**, 1348 (2006)
12. K. Wang, W. Li, W. Xu, S. Hou, S. Hu (2020). <https://doi.org/10.1007/s12540-020-00669-x>
13. S.-Z. Lu, A. Hellawell, *Metall. Trans. A* **18**, 1721 (1987)
14. P. Srirangam, S. Chattopadhyay, A. Bhattacharya, S. Nag, J. Kaduk, S. Shankar, R. Banerjee, T. Shibata, *Acta Mater.* **65**, 185 (2014)
15. W. Yi, J. Gao, Y. Tang, L. Zhang, *Calphad* **68**, 101732 (2020)
16. I.N. Ganiev, A.V. Zakhobov, T.D. Dzhuraev, *Izv. A. N. SSSR (Metally)* **9**, 215 (1977)
17. A.V. Vakhobov, T.D. Dzhuraev, I.N. Ganiev, *Zavod. Lab.* **43**, 73 (1977)
18. M.D. Hanna, A. Hellawell, *MRS Online Proc. Libr.* **19**, 411 (1983)
19. E. Sato, N. Kono, H. Watanabe, I. Sato, *J. Japan Inst. Light Met.* **35**, 71 (1985)
20. A.M. Garay-Tapia, A.H. Romero, G. Trapaga, R. Arróyave, *Intermetallics* **21**, 31 (2012)
21. S.M. Kauzlarich, C.L. Condrion, J.K. Wassei, T. Ikeda, G.J. Snyder, *J. Solid State Chem.* **182**, 240 (2009)
22. P.D. Lee, S. Sridhar, *Int. J. Cast Metal. Res.* **13**, 185 (2000)
23. X. Bian, Z. Zhang, X. Liu, *Mater. Sci. Forum*, **331–337**, 361 (2000)
24. H.C. Liao, W. Song, Q.G. Wang, L. Zhao, R. Fan, F. Jia, *Int. J. Cast Metal. Res.* **26**, 201 (2013)
25. A.M. Samuel, H.W. Doty, S. Valtierra, F.H. Samuel, *Int. J. Met-alcast.* **11**, 729 (2017)
26. W. Zhang, S. Ma, Z. Wei, P. Bai, *Materials* **12**, 3222 (2019)
27. S.M. Miresmaeili, S.G. Shabestari, S.M.A. Boutorabi, *Int. J. Cast Met. Res.* **16**, 541 (2003)
28. C. Lee, *Mater. Sci. Eng. A* **776**, 138992 (2020)
29. T. Liu, S. Morales, M. Karkkainen, L. Nastac, V. Arvikar, I. Levin, L.N. Brewer, *Mater. Sci. Eng. A* **756**, 373 (2019)
30. W. Schneller, M. Leitner, S. Springer, F. Grun, M. Taschauer, *J. Manuf. Mater. Process.* **3**, 16 (2019)
31. C.J. Davidson, J.R. Griffiths, A.S. Machin, *Fatigue Fract. Eng. M.* **25**, 223 (2002)
32. J. Lee, H.J. Bong, D. Kim, Y.S. Lee, Y. Choi, M.G. Lee, *Met. Mater. Int.* **26**, 682 (2020)
33. M. Palacz, B. Melka, B. Wecki, G. Siwec, R. Przylucki, P. Bulinski, S. Golak, L. Blacha, J. Smolka, *Met. Mater. Int.* **26**, 695 (2020)
34. A.P. Sekhar, D. Das, *Met. Mater. Int.* **27**, 337 (2021)
35. G. Ranjbari, A. Doniavi, M. Shahbaz, R. Ebrahimi, *Met. Mater. Int.* **27**, 683 (2021)
36. I.K. Duygun, O. GURSOY, E. Erzi, D. Dispınar, in *Shape Casting: 7th International Symposium Celebrating Prof. John Campbell's 80th Birthday*, ed. by M. Tiryakiođlu, W. Griffiths, M. Jolly (The Minerals, Metals & Materials Series. Springer, Cham, 2019), pp. 353–361
37. L. Liu, A.M. Samuel, F.H. Samuel, H.W. Doty, S. Valtierra, *J. Mater. Sci.* **39**, 215 (2004)
38. A. Fortini, L. Lattanzi, M. Merlin, G.L. Garagnani, *Int. J. Met-alcast.* **12**, 697 (2018)
39. H. Liao, Y. Sun, G. Sun, *Mater. Sci. Eng. A* **335**, 62 (2002)
40. N. Habibi, A.M. Samuel, F.H. Samuel, P. Rochette, D. Paquint, *Int. J. Cast Met. Res.* **17**, 79 (2004)
41. M.A. Moustafa, F.H. Samuel, H.W. Doty, S. Valtierra, *Int. J. Cast Met. Res.* **14**, 235 (2002)
42. F.J. Tavitias-Medrano, J.E. Gruzleski, F.H. Samuel, S. Valtierra, H.W. Doty, *Mater. Sci. Eng. A* **480**, 356 (2008)
43. F. Paray, J.E. Gruzleski, *Mater. Sci. Technol.* **10**, 757 (1994)
44. Y. Uchida, T. Toyama, A. Tsuruno, T. Izumi, *J. Japan Inst. Light Met.* **68**, 299 (2018)
45. E. Yanagihara, G. Aoshima, S. Komura, S. Saikawa, S. Ikeno, *Mater. Sci. Forum* **879**, 2383 (2017)
46. M. Uludađ, M. Kocabař, D. Dıřplnar, R. Cetin, N. Cansever, *Arch. Foundry Eng.* **17**, 125 (2017)
47. Y.T. Liu, J.X. Lin, X.P. Wu, L.Y. Niu, G.Y. Li, *Adv. Mater. Res.* **750–752**, 638 (2013)
48. M. Marzouk, M. Jain, S. Shankar, *Mater. Sci. Eng. A* **598**, 277 (2014)
49. A.P. Hekimođlu, M. alıř, G. Ayata, *Met. Mater. Int.* **25**, 1488 (2019)
50. J. Zhang, Z.Y. Pang, C.C. Sun, N. Liu, H.M. Chen, *Mater. Sci. Forum* **993**, 12 (2020)
51. P. Srirangam, M.J. Kramer, S. Shankar, *Acta Mater.* **59**, 503 (2011)
52. A. Kosa, Z. Gacsi, J. Dul, *J. Mater. Sci. Eng.* **37**, 43 (2012)
53. O.A. Atasoy, H.E. Exner, *Cast Met.* **1**, 86 (1988)
54. T.S. Shih, F.S. Shih, *Int. J. Cast Metal. Res.* **10**, 273 (1998)
55. O. Elsebaie, A.M. Samuel, F.H. Samuel, *J. Mater. Sci.* **46**, 3027 (2011)
56. İ. Öztürk, G.H. Ađaođlu, E. Erzi, D. Dispınar, G. Orhan, *J. Alloy. Compd.* **763**, 384 (2018)
57. H.C. Liao, W.R. Huang, M.D. Cai, *Int. J. Cast Metal. Res.* **24**, 102 (2011)
58. A.K. Dahle, K. Nogita, S.D. McDonald, J.W. Zindel, L.M. Hogan, *Metall. Mater. Trans. A* **32**, 949 (2001)
59. K. Nogita, A.K. Dahle, *Mater. Trans.* **42**, 207 (2001)
60. X. Liu, B. Beausir, Y. Zhang, W. Gan, H. Yuan, F. Yu, C. Esling, X. Zhao, L. Zuo, *J. Alloy. Compd.* **730**, 208 (2018)
61. G. Huber, M.B. Djurdjevic, M. Rafetzeder, *Mater. Sci. Forum* **879**, 784 (2017)
62. A.M.A. Mohamed, F.H. Samuel, A.M. Samuel, H.W. Doty, *Mater. Des.* **30**, 4218 (2009)
63. A.T. Joenoes, J.E. Gruzleski, *Cast Met.* **4**, 62 (1991)
64. M. Uludađ, M. Uyaner, F. Yılmaz, D. Dıřpınar, *Arch. Foundry Eng.* **15**, 134 (2015)
65. M. Timpel, N. Wanderka, G.S. Vinod Kumar, J. Banhart, *Ultra-microscopy* **111**, 695 (2011)
66. S. Haro-Rodriguez, R.E. Goytia-Reyes, D.K. Dwivedi, V.H. Baltazar-Hernandez, H. Flores-Zuniga, M.J. Perez-Lopez, *Mater. Design* **32**, 1865 (2011)
67. L. Hengcheng, S. Yu, S. Guoxiong, *Mater. Sci. Eng. A* **358**, 164 (2003)
68. M. Timpel, N. Wanderka, R. Schlesiger, T. Yamamoto, N. Lazarev, D. Isheim, G. Schmitz, S. Matsumura, J. Banhart, *Acta Mater.* **60**, 3920 (2012)
69. B. Atakav, O. GURSOY, E. Erzi, K. Tur, D. Dispınar, *Mater. Res. Express* **7**, 026549 (2020)
70. B.B. Stunova, *Acta Polytech.* **52**, 26 (2012)
71. B. Closset, J.E. Gruzleski, *Metall. Trans. A* **13**, 945 (1982)
72. M. Zarif, B. McKay, P. Schumacher, *Metall. Mater. Trans. A* **42**, 1684 (2011)
73. İ.K. Duygun, G.H. Ađaođlu, D. Dispınar, G. Orhan, *J. Alloy. Compd.* **803**, 786 (2019)
74. S. McDonald, M. Dargusch, G. Song, D. StJohn, in *Shape Casting: 2nd International Symposium*, ed. by P.N. Crepeau, M. Tiryakiođlu, J. Campbell (TMS Publishing Company, Pittsburgh, 2007), pp. 59–66
75. M. Wang, J.C. Pang, H.Q. Liu, S.X. Li, Z.F. Zhang, *J. Mater. Res. Technol.* **8**, 4556 (2019)
76. P. Nelaturu, S. Jana, R.S. Mishra, G. Grant, B.E. Carlson, *Mater. Sci. Eng. A* **780**, 139175 (2020)
77. D.A. Lados, D. Apelian, *Eng. Fract. Mech.* **75**, 821 (2008)
78. S. Jana, R.S. Mishra, J.B. Baumann, G. Grant, *Scripta Mater.* **61**, 992 (2009)
79. S. Jana, R.S. Mishra, J.B. Baumann, G. Grant, *Acta Mater.* **58**, 989 (2010)

80. S.W. Han, S.W. Kim, *Met. Mater. Int.* **10**, 13 (2004)
81. S.Z. Lu, A. Hellawell, *J. Cryst. Growth* **73**, 316 (1985)
82. D. Emadi, J.E. Gruzleski, J.M. Toguri, *Metall. Trans. B* **24**, 1055 (1993)
83. C.M. Dinnis, A.K. Dahle, J. A. Taylor, M.O. Otte, *Metall. Mater. Trans. A* **35**, 3531 (2004)
84. D. Dispinar, S. Akhtar, A. Nordmark, M. Di Sabatino, L. Arnerberg, *Mater. Sci. Eng. A* **527**, 3719 (2010)
85. D. Dispinar, J. Campbell, *Int. J. Cast Met. Res.* **17**, 280 (2004)
86. N.S. Tiedje, J.A. Taylor, M.A. Easton, *Metall. Mater. Trans. A* **43**, 4846 (2012)
87. S.L. Lee, Y.C. Cheng, W.C. Chen, C.K. Lee, A.H. Tan, *Mater. Chem. Phys.* **135**, 503 (2012)
88. W.R. Osorio, L.R. Garcia, P.R. Goulart, A. Garcia, *Mater. Chem. Phys.* **106**, 343 (2007)
89. E. McCafferty, *Corros. Sci.* **45**, 1421 (2003)
90. M.F. Hafiz, T. Kobayashi, *J. Japan Inst. Light Met.* **44**, 28 (1994)
91. J.P.G. Ferreira, L.A. Lourencato, A.S. Roca, H.D.C. Fals, *Metall. Mater. Trans. A* **51**, 6421 (2020)
92. Q.G. Wang, D. Apelian, D.A. Lados, *J. Light Met.* **1**, 85 (2001)
93. P. Nelaturu, S. Jana, R.S. Mishra, G. Grant, B.E. Carlson, *Mater. Sci. Eng. A* **716**, 165 (2018)
94. S.R. Sharma, Z.Y. Ma, R.S. Mishra, *Scripta Mater.* **51**, 237 (2004)
95. R. Chen, Q. Xu, Z. Jia, B. Liu, *Mater. Design* **90**, 1059 (2016)
96. W. Jiang, X. Xu, Y. Zhao, Z. Wang, C. Wu, D. Pan, Z. Meng, *Mater. Sci. Eng. A* **721**, 263 (2018)
97. M. Kim, *Met. Mater. Int.* **13**, 103 (2007)
98. C. Li, Y. Pan, T. Lu, L. Jing, J. Pi, *Met. Mater. Int.* **24**, 1133 (2018)
99. S.M. Jigajinni, K. Venkateswarlu, S.A. Kori, *Met. Mater. Int.* **19**, 171 (2013)
100. L. Qiyang, L. Qingchun, L. Qifu, *Acta Metall. Mater.* **39**, 2497 (1991)
101. M.M. Makhlof, H.V. Guthy, *J. Light Met.* **1**, 199 (2001)
102. S. Hegde, K.N. Prabhu, *J. Mater. Sci.* **43**, 3009 (2008)
103. M. Shamsuzzoha, L. M. Hogan, *Philos. Mag. A* **54**, 459 (1986)
104. D.R. Hamilton, R.G. Seidensticker, *J. Appl. Phys.* **31**, 1165 (1960)
105. K.F. Kobayashi, L.M. Hogan, *J. Mater. Sci.* **20**, 1961 (1985)
106. Z. Yu, X. Fu, J. Zhu, *Cryst. Growth Des.* **14**, 4411 (2014)
107. L. Clapham, Ph.D. Thesis, Queens University (1987)
108. S.C. Flood, J.D. Hunt, *Met. Sci.* **15**, 287 (1981)
109. H. Fredriksson, M. Hillert, N. Lange, *J. Inst. Met.* **101**, 285 (1973)
110. A.K. Dahle, Formation of eutectic in hypoeutectic Al-Si alloys and its effect on porosity formation, in *Proceedings of the Joint Australia-Korea Workshop on Light Alloys, Jeju*, 25–26 May 2000 (KOSEF and Australia Academy of Science, Pohang, 2000), p. 70
111. W. Wang, X. Bian, J. Qin, S.I. Sliusarenko, *Acta Metall. Sin.* **34**, 645 (1998)
112. X.F. Bian, W.M. Wang, J.Y. Qin, *Mater. Sci. Forum* **331–337**, 349 (2000)
113. S. Shankar, Y.W. Riddle, M.M. Makhlof, *Acta Mater.* **52**, 4447 (2004)
114. K. Nogita, S.D. McDonald, K. Tsujimoto, K. Yasuda, A.K. Dahle, *J. Electron Microsc.* **53**, 361 (2004)
115. S.M. Liang, R. Schmid-Fetzer, *Acta Mater.* **72**, 41 (2014)
116. G.K. Sigworth, *Int. J. Metalcast.* **2**, 19 (2008)
117. J. Campbell, *Metall. Mater. Trans. B* **37**, 857 (2006)
118. G. Timelli, D. Caliarì, J. Rakhmonov, *J. Mater. Sci. Technol.* **32**, 515 (2016)
119. X. Cao, J. Campbell, *Metall. Mater. Trans. A* **35**, 1425 (2004)
120. C.D. Lee, *Met. Mater. Int.* **27**, 900 (2021)
121. L. Liu, A.M. Samuel, F.H. Samuel, H.W. Doty, S. Valtierra, *Int. J. Met.* **11**, 729 (2017)
122. H. Shahani, *Scand. J. Metall.* **14**, 306 (1985)
123. D. Wei, R. Liu, C. Zuo, H. Zhou, *Met. Mater. Int.* **26**, 739 (2020)
124. C.R. Barbosa, G.H. Machado, H.M. Azevedo, F.S. Rocha, J.C. Filho, A.A. Pereira, O.L. Rocha, *Met. Mater. Int.* **26**, 370 (2020)
125. G.S. Ham, M.S. Baek, J.H. Kim, S.W. Lee, K.A. Lee, *Met. Mater. Int.* **23**, 35 (2017)
126. M. Uludağ, L. Gemi, M.R. Eryilmaz, D. Dispinar, The effect of Sr modification and holding time on microstructure of hypereutectic Al-Si alloy, in *Proceedings of the 17th International Metallurgy & Materials Congress (IMMC)*, Istanbul, 11–13 September 2014, p. 942
127. M. Wang, J.C. Pang, S.X. Li, Z.F. Zhang, *Mater. Sci. Eng. A* **704**, 480 (2017)
128. S.W. Kim, U.J. Lee, S.W. Han, *Met. Mater. Int.* **9**, 157 (2003)
129. C.C. Hsu, J.Y. Wang, J.J. Huang, S. Lee, *Met. Mater. Int.* **18**, 567 (2012)
130. B. Sagbas, *Met. Mater. Int.* **26**, 143 (2020)
131. K.V. Shankar, M. Balachandran, B.S. Pillai, S.R. Krishnan, N.S. Harikrishnan, A.R. Harinarayanan, V.S. Kumar, *J. Bio. Tribo. Corros.* **7**, 96 (2021). <https://doi.org/10.1007/s40735-021-00531-6>

Publisher's Note Springer Nature remains neutral with regard to jurisdictional claims in published maps and institutional affiliations.